CANCER

Edge modification facilitated heterogenization and exfoliation of two-dimensional nanomaterials for cancer catalytic therapy

Liqun Chen[1]†, Zhuo Mao[1,3]†, Yang Wang[2]†, Yong Kang[1], Ying Wang[2], Lin Mei[3], Xiaoyuan Ji[1]*

The rapid recombination of electron-hole pairs and limited substrates are the most critical factors astricting the effect of catalytic therapy. Thus, two-dimensional interplanar heterojunction ($BiOCl/Bi_2O_3$) that prolongs the lifetime of excited electrons and holes and extends the selectivity of substrates under ultrasound irradiation is prepared to facilitate high-performance cancer therapy. An edge modification displacing marginal BiOCl to Bi_2O_3 is proposed to construct the interplanar heterojunction, promoting ultrathin nanosheets exfoliation due to the enhanced edge affinity with H_2O. The spontaneously aligning Fermi levels mediate a built-in electric field–guided Z-scheme interplanar heterojunction, retard electron-hole pairs recombination, and improve redox potentials. Hence, these high-powered electrons and holes are capable of catalyzing diverse and stable substrates, such as the reduction reactions, $O_2 \rightarrow \cdot O_2^-$ and $CO_2 \rightarrow CO$, and oxidation reactions, $GSH \rightarrow GSSG$ and $H_2O \rightarrow \cdot OH$. The Z-scheme interplanar heterojunction with the extending substrates selectivity completely breaks the tumor microenvironment limitation, exhibiting high anticancer activity.

INTRODUCTION

Catalysis is an omnipotent "tool" creating an enchanting world for human survival and development through millions of years of evolution (*1*–*6*). Recently, the combination of catalysis and medicine, viz., catalytic medicine, integrates catalytic technology to solve medical problems. Moreover, it provides efficient treatment strategies against various pathological abnormalities, including cancer, bacterial infection, inflammation, and other diseases (*7*–*10*). Undoubtedly, the physical and chemical properties of the catalyst, such as activity, selection, and stability, are integral to the curative effect of catalytic medicine.

Three crucial factors and steps essentially determine the catalytic efficiency in medicine applications, namely, (i) excitation energy (light or ultrasound) absorption, (ii) electron-hole pairs separation and migration from the bulk to the surface, and (iii) surface catalysis reactions (*11*–*14*). The mainly used catalytic medicine focuses on reactive oxygen species (ROS) generation from O_2- or H_2O_2-induced oxidative damage to cancer cells (*15*). Nevertheless, the effect of these redox imbalance–based catalytic therapies is extremely limited by the unique tumor microenvironment (TME). For instance, hypoxia and limited H_2O_2 concentration restrict the ROS generation efficacy, and high expression glutathione (GSH) and peroxidase consume ROS (*16*–*20*). Therefore, developing previously unidentified cancer catalytic medicine is desired, notably expanding the range of substrates and therapeutic products.

On the basis of the perspective of catalytic chemistry, the catalyst must have a high valence band (VB) and conduction band (CB) levels with enough redox potential energy to broaden the range of substrates and therapeutic products (*11*, *13*, *21*, *22*). However, the bandgap, the energy level difference between VB and CB, will increase with the increase of VB and CB levels, which would inevitably lead to the difficulty of separating electron-hole pairs and poor catalytic activity (*23*). Therefore, there is an irreconcilable contradiction between broadening the catalytic reaction type and the catalytic activity for a single catalyst (*14*).

The construction of heterojunction is one of the most practical and effective strategies to break through this contradiction, simultaneously accelerating the separation of the electron-hole pairs and extending the species of substrate and therapeutic product selection (*23*–*27*). Z-scheme heterojunction with excellent properties of natural photosynthesis owns many advantages over single catalysts and other types of heterojunctions. Two photosensitizers are activated simultaneously, and the electrons within the lower CB of one photosensitizer combine with the lower VB of the other so that the higher CB and VB of these photosensitizers would have separated electrons and holes having high reduction/oxidation potentials (*23*, *25*, *28*, *29*). The primary advantage of biomimetic Z-scheme heterojunction is that it improves the separation efficiency of charges and promotes reduction and oxidation potentials, directly broadening the catalytic reaction range and activity.

Two-dimensional (2D) nanomaterials representing a previously unidentified class of nanomaterials have been exhaustively used in developing catalysis due to their sizeable bandgap, good conductivity, fast electron transfer, and photoelectrochemical activity (*30*–*37*). In particular, 2D heterostructures integrating the advantages of 2D nanomaterials and heterojunction are conducive to elevating energy conversion capacity and improving oxidation and reduction (*11*, *13*, *21*, *22*). Here, a 2D interplanar Z-scheme heterojunction ($BiOCl/Bi_2O_3$) was developed through a smart wet-chemical method integrating interplanar heterojunction synthesis and 2D ultrathin heterojunction exfoliation within one step. As exhibited in Fig. 1, after the bulk layered bismuth oxychloride (BiOCl) was synthesized using a hydrothermal process, the edges of BiOCl were selectively

[1]Academy of Medical Engineering and Translational Medicine, Medical College, Tianjin University, Tianjin 300072, China. [2]School of Pharmaceutical Sciences (Shenzhen), Sun Yat-sen University, Guangzhou 510275, China. [3]Tianjin Key Laboratory of Biomedical Materials, Key Laboratory of Biomaterials and Nanotechnology for Cancer Immunotherapy, Institute of Biomedical Engineering, Chinese Academy of Medical Sciences and Peking Union Medical College, Tianjin 300192, China.
*Corresponding author. Email: jixiaoyuan@tju.edu.cn
†These authors contributed equally to this work.

modified and transformed into Bi_2O_3, which constructed an interesting interplanar heterojunction. Moreover, it also facilitated the exfoliation by improving affinity with water molecules. At this interplanar heterojunction BiOCl/Bi_2O_3 nanosheets (NSs) interface, a built-in electric field was formed by the aligning Fermi levels of BiOCl and Bi_2O_3, guiding excited electron and hole redistribution. Using US irradiation, the ultrasound (US)–excited electrons on the CB of Bi_2O_3 will be combined with the holes on the VB of BiOCl, using the driving force of the built-in electric field in their interface, leaving stronger reduction/oxidation potentials of separated electrons and holes over the CB of BiOCl and the VB of Bi_2O_3, respectively. Hence, a built-in electric field–facilitated Z-schemed catalytic mechanism was constructed, which endowed that the electrons and holes were separated thoroughly and had the most powerful reduction and oxidation potentials, respectively. Thus, two active catalytic sites located at the CB of BiOCl and the VB of Bi_2O_3 were capable of catalyzing both conventional reactions, such as $O_2 + e^- \rightarrow \cdot O_2^-$ and $GSH + h^+ \rightarrow GSSG$, and difficult reactions, such as $CO_2 + 2H^+ + 2e^- \rightarrow CO + H_2O$ and $H_2O + h^+ \rightarrow \cdot OH + H^+$. The extension of substrates and therapeutic products based on the 2D interplanar Z-scheme heterojunction breaks the limitation of the TME to catalytic therapy. It exhibits excellent antitumor performance both in vitro and in vivo. Hence, this work provides a smart strategy to intelligently synthesize 2D ultrathin heterojunction and an advanced strategy to enhance the efficiency and application range of catalytic therapy by increasing the selectivity of nanocatalysts.

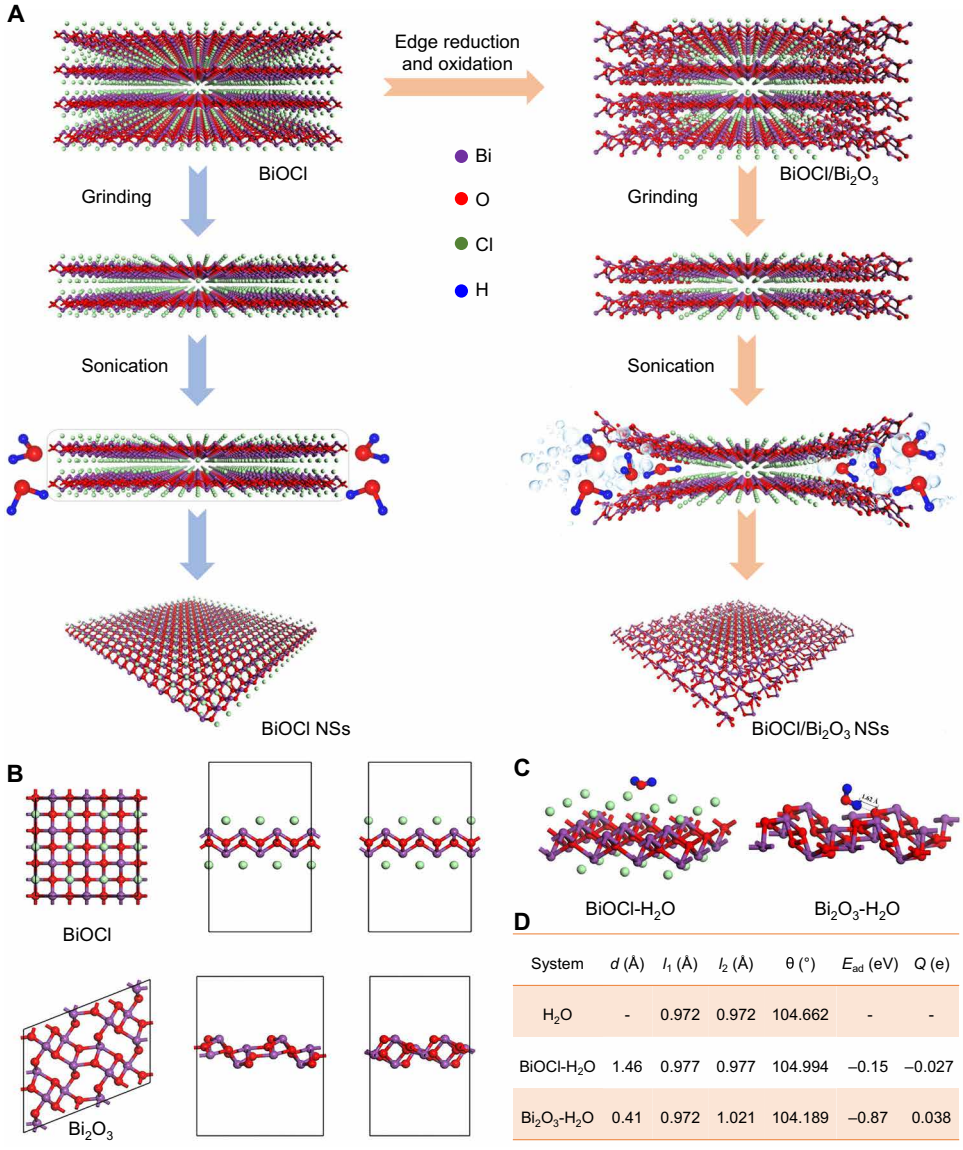

System	d (Å)	l_1 (Å)	l_2 (Å)	θ (°)	E_{ad} (eV)	Q (e)
H_2O	-	0.972	0.972	104.662	-	-
BiOCl-H_2O	1.46	0.977	0.977	104.994	–0.15	–0.027
Bi_2O_3-H_2O	0.41	0.972	1.021	104.189	–0.87	0.038

Fig. 1. Schematic illustration of the edge selective modification preparation facilitated exfoliation and heterogenization of the 2D nanomaterials (BiOCl/Bi_2O_3 NSs) by extending catalytic selectivity to bypass the TME restrictions. (**A**) BiOCl/Bi_2O_3 NS preparation with Z-schemed heterojunction. (**B**) Top and side views of the fully optimized BiOCl and Bi_2O_3 NSs. (**C**) Optimized geometries of H_2O molecule on the surface of BiOCl and Bi_2O_3 NSs. (**D**) Equilibrium distance (d) between the NS and H_2O. The intramolecular bond angle (θ) and bond length (l_1 and l_2) of H_2O, respectively. The adsorption energy (E_{ad}) and charge transfer (Q) for each adsorption system.

RESULTS

Preparation and characterization of BiOCl/Bi_2O_3 NS-based interplanar heterojunction

The layered BiOCl powder was synthesized using a hydrothermal process applying $Bi(NO_3)_3{\cdot}5H_2O$ as the substrate (fig. S1A). Subsequently, the interplanar heterojunction BiOCl/Bi_2O_3 was synthesized through in situ reductions and oxidation of layered BiOCl powder (fig. S1B). After being immersed in KBH_4 for 10 min, the edges of layered BiOCl powder were reduced to Bi (Fig. 1). Then, the Bi edges of BiOCl were oxidized to Bi_2O_3 after reacting with H_2O_2. The change in color from white (BiOCl) to faint yellow (BiOCl/Bi_2O_3) depicted the first evidence of successful BiOCl/Bi_2O_3 synthesis (fig. S1). Next, the BiOCl NSs and BiOCl/Bi_2O_3 NSs were liquid exfoliated in water under ultrasonic treatment to avoid additional toxicity from organic solvents. BiOCl/Bi_2O_3 is much easier to peel off in an aqueous solution than BiOCl. However, for exfoliation of BiOCl NSs in water solution, 12-hour ultrasonic treatment was required for nanoscale BiOCl NSs. Hence, the edge modification not only constructed an interplanar heterojunction but also facilitated the exfoliation of layered NSs. The mechanism of this exciting phenomenon is illustrated in Fig. 1. As shown in Fig. 1B, the models for BiOCl and Bi_2O_3 were established with supercells of $3 \times 3 \times 1$ and $2 \times 2 \times 1$ unit cells, respectively. Inside the sandwich layer structure of BiOCl, Cl atoms were distributed on both sides of the Bi_2O_2 layer. The average distance between Cl and O was 3.30 Å. Bi_2O_3 had a network structure with eight-membered and four-membered rings having alternating Bi and O atoms. The calculated layer thickness was 2.91 Å. After edge modification, the distance between each layer did not change significantly. Since the vibration of solvent molecules (H_2O) in response to US is the main force that breaks the layered structure of the compound, we hypothesized that hydrophilicity could be the main reason for the difficulty in exfoliation. Therefore, the adsorption of H_2O on BiOCl and Bi_2O_3 was investigated to predict the hydrophilic property of BiOCl and Bi_2O_3. Figure 1C shows the most stable configurations of H_2O adsorption systems. The equilibrium distance, the intramolecular bond length, bond angle of H_2O before and after adsorption, the adsorption energy, and charge transfer for each system are given in Fig. 1D. We observed that the H_2O-Bi_2O_3 system had a smaller equilibrium distance of 0.41 Å and a much lower adsorption energy of −0.87 eV. These findings indicated that Bi_2O_3 are more hydrophilic than BiOCl. The intermolecular hydrogen bond forming contributes to the high affinity between Bi_2O_3 and H_2O after H_2O exposure. Therefore, the improved hydrophilicity of BiOCl/Bi_2O_3 may be more conducive to the exfoliation of ultrathin NSs in water.

As exhibited in Fig. 2A, the size of the prepared BiOCl powder was about 1000 nm, and the layered structure was revealed in the scanning electron microscope (SEM) image of BiOCl. After 12 hours of continuous sonication, the BiOCl NSs with a thickness of 10- and 176-nm size were prepared (Fig. 2, B and C, and figs. S2A and S3A). The high-resolution transmission electron microscopy (HRTEM) images of BiOCl NSs were observed in Fig. 2D. A clear interference fringe and *d*-spacing of 0.73 nm was corresponding to the plane of BiOCl. For BiOCl/Bi_2O_3 NSs, after edge modification, the edges of BiOCl/Bi_2O_3 began to curl, and the layered structure became more evident (Fig. 2E). A thickness of 6 nm and a size of 156 nm of BiOCl/Bi_2O_3 NSs were obtained after 5 hours of ultrasonic treatment (Fig. 2, F and G, and figs. S2B and S3B). The HRTEM images revealed the clear interference fringe and *d*-spacing of 0.73 and 0.33 nm, corresponding to the plane of BiOCl NSs and Bi_2O_3 NSs (Fig. 2H). Next, x-ray photoelectron spectroscopy (XPS), x-ray diffractometry (XRD), and Raman spectra analyzed the chemical composition and structures of as-prepared BiOCl NSs and BiOCl/Bi_2O_3 NSs. In the XRD spectra of BiOCl/Bi_2O_3 NSs (Fig. 2I), two respective crystal structures were observed, corresponding with the tetragonal structure of BiOCl [Joint Committee on Powder Diffraction Standards (JCPDS) no. 06-0249] and the monoclinic structure of Bi_2O_3 (JCPDS no. 06-0294). In the Raman spectra (Fig. 2J), BiOCl NSs showed two distinctive bands at 144 cm^{-1} (assigned to A_{1g} internal Bi-Cl stretching mode) and 197 cm^{-1} (assigned to E_g internal Bi-Cl stretching mode). After edge modification, the characteristic peaks of Bi_2O_3 were exhibited in the spectrum of BiOCl/Bi_2O_3 NSs. The 119-cm^{-1} modes came from Ag symmetry caused primarily by the participation of Bi atoms. Modes of 138 (A_g) and 153 cm^{-1} (B_g) could come from the displacements of both Bi and O atoms in the Bi_2O_3 lattice. The Raman peaks with the higher-frequency modes 183, 211, 279, 313, 410, 446, and 521 cm^{-1} were attributed to the displacements of the O atoms in Bi_2O_3. During the XPS analysis (Fig. 2K), the specific peaks of Bi 4f, O 1s, and Cl 2p were observed. As shown in Fig. 2 (L and M), the typical high-resolution XPS spectra of Cl 2p of BiOCl NSs were much higher than that of BiOCl/Bi_2O_3 NSs. For typical high-resolution XPS spectra of Bi 4f of BiOCl/Bi_2O_3 NSs, other than the specific peaks of Bi 4f from BiOCl NSs, two other specific peaks of Bi 4f from Bi_2O_3 NSs were also observed. More obvious evidence was demonstrated in the high-resolution XPS spectra of O 1s. As shown in Fig. 2 (P and Q), apart from these specific peaks of O 1s BiOCl NSs and absorbed O_2, another specific peak of O 1s of Bi_2O_3 NSs was also observed. These characterizations further demonstrated the successful edge modification. Biocompatibility and dispersibility are crucial for biomedical applications. The as-prepared BiOCl NSs and BiOCl/Bi_2O_3 NSs were modified using polyethylene glycol 5k [PEG(5k)]–NH_2 through electrostatic attraction between positively charged PEG(5k)-NH_2 and negatively charged NSs (fig. S4). Moreover, thermogravimetric analysis was applied to quantify the PEG(5k)-NH_2 coated on the surface of the NSs [≈20.3% (w/w)] (fig. S5). PEGylation of BiOCl NSs and BiOCl/Bi_2O_3 NSs improved dispersion in water, phosphate-buffered saline (PBS), and cell culture medium than with the bare NSs (fig. S6 and table S1). Enhanced dispersion in a solution would provide more active sites of catalysts. Moreover, the improved hydrophilia would decrease the distance between catalysts and substrates, notably improving the catalytic reaction rate. Therefore, PEGylation is essential for nanomedicine used in vivo and the catalytic properties, and in vitro and in vivo experiments were carried out after PEGylation of BiOCl NSs and BiOCl/Bi_2O_3 NSs. Fourier transform infrared absorption bands of the PEGylated BiOCl/Bi_2O_3 NSs at ~2900 and ~1250 cm^{-1} corresponded to the —CH and C═O stretching vibration in the PEG-NH_2 segment (fig. S7). The energy dispersive spectrometer (EDS) mappings observed in Fig. 2 (R and S) exhibited a homogeneous Bi, O, and Cl distribution in BiOCl NSs. They reduced the concentration of Cl in BiOCl/Bi_2O_3 NSs. Moreover, the ratio of BiOCl to Bi_2O_3 in prepared BiOCl/Bi_2O_3 NSs was determined. As shown in table S2, after edge modification, the atomic percent of Bi in BiOCl/Bi_2O_3 NSs was consistent with that in BiOCl NSs, without any impurities during edge modification. The atomic percent of Cl decreased from 31.32 to 23.38%, converting nearly 25.35% of BiOCl to Bi_2O_3. Hence, the ratio of BiOCl to Bi_2O_3 in prepared BiOCl/Bi_2O_3 NSs was evaluated to be 2.94:1. In addition, from the

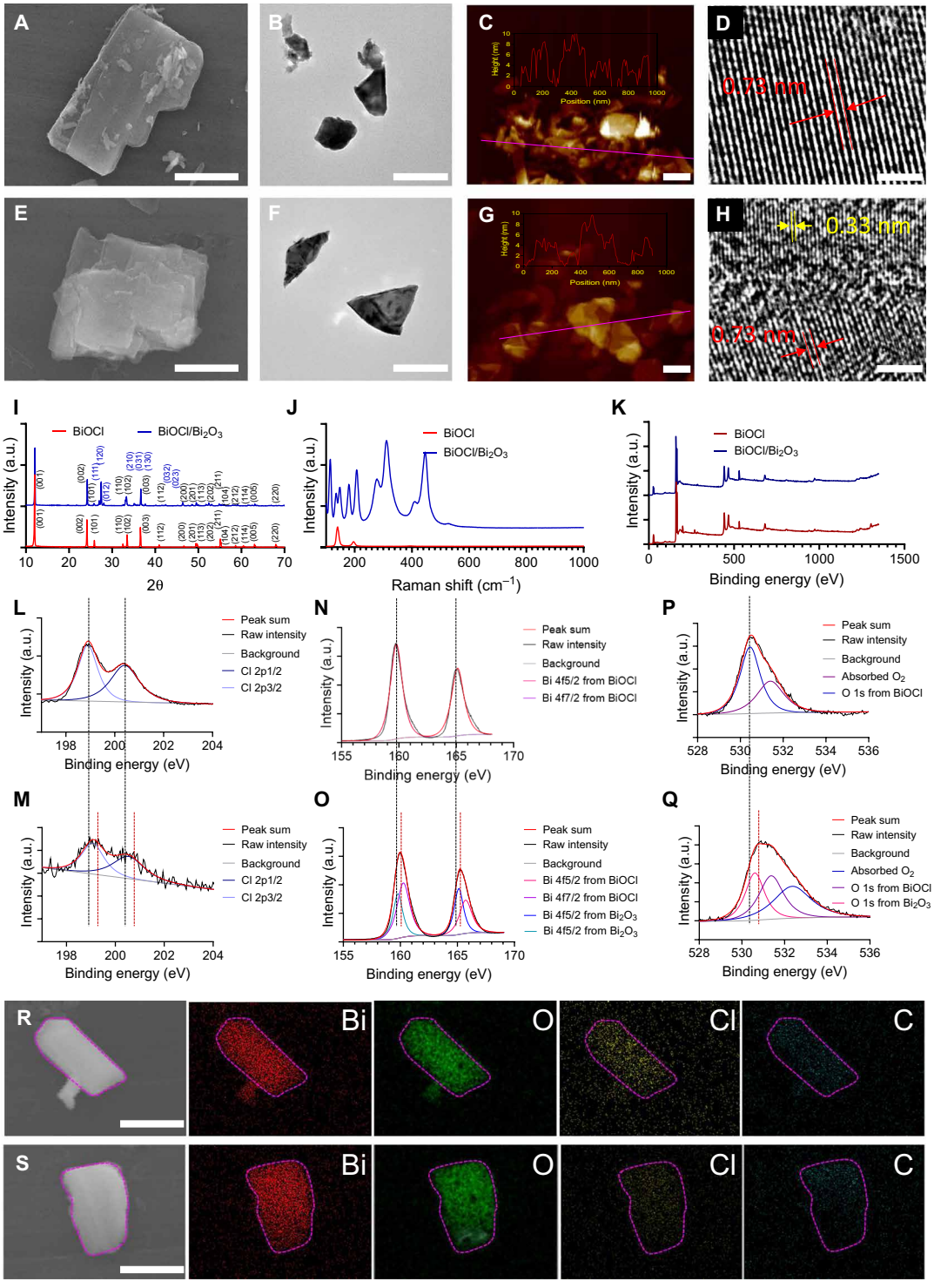

Fig. 2. Characterization of BiOCl/Bi_2O_3 NSs. (**A**) SEM, (**B**) TEM, (**C**) 2D atomic force microscopy (AFM), and (**D**) HRTEM images of BiOCl NSs. (**E**) SEM, (**F**) TEM, (**G**) 2D AFM, and (**H**) HRTEM images of BiOCl/Bi_2O_3 NSs. (**I**) XRD, (**J**) Raman, and (**K**) XPS spectra of BiOCl NSs and BiOCl/Bi_2O_3 NSs. HRXPS spectra of (**L**) Cl, (**N**) Bi, and (**P**) O of BiOCl NSs. HRXPS spectra of (**M**) Cl, (**O**) Bi, and (**Q**) O of BiOCl/Bi_2O_3 NSs. Energy dispersive spectrometer (EDS) mapping of the (**R**) BiOCl NSs and (**S**) BiOCl/Bi_2O_3 NSs. Scale bars, 1000 nm (A and E), 100 nm (B, C, F, G, R, and S), 5 nm (D and H). a.u., arbitrary units.

viewpoint of practical applications, the stability of the $BiOCl/Bi_2O_3$ NSs within different acidic solutions (pHs 5.0, 7.4, and 8.0) was analyzed. As shown in fig. S8, after being immersed in the above solutions for 48 hours, the morphology and structure of NSs did not alter obviously. The XPS, XRD, and Raman spectra of $BiOCl/Bi_2O_3$ NSs remained nearly the same before and after 48 hours of acid and alkaline environment treatments (fig. S9), demonstrating the notable stability of prepared $BiOCl/Bi_2O_3$ NSs.

Analysis of catalytic performance and mechanism

Specific catalysis is one of the excellent properties of catalysts (*38*–*40*). However, because of the lack of substrate concentration in the TME, the application of catalysts with high specificity is limited (*41*–*43*). Therefore, broadening the catalytic selectivity of catalysts could achieve the efficiency of catalytic medicine. First, diphenyl isobenzofuran (DPBF) as a $\cdot O_2^-$ probe was applied to detect the $\cdot O_2^-$ generation through O_2 reduction (Fig. 3A). As shown in Fig. 3B and fig. S10, the treatment through US, BiOCl NSs, and $BiOCl/Bi_2O_3$ NSs alone could not generate $\cdot O_2^-$. Coupling NS-based catalyst and US, different content $\cdot O_2^-$ was developed, in which $BiOCl/Bi_2O_3$ NSs depicted stronger $\cdot O_2^-$-generating ability than BiOCl NSs. The $\cdot O_2^-$-rendering performance was detected under BiOCl NSs + US and $BiOCl/Bi_2O_3$ NSs + US treatments within a hypoxic environment to verify that O_2 is the substrate of $\cdot O_2^-$ and simulate a hypoxic TME in vitro. Much less $\cdot O_2^-$ yields were obtained and exhibited in Fig. 3B. Second, the CO yield developed from CO_2 reduction was determined qualitatively and quantitatively using myoglobin and gas chromatography (Fig. 3C). Similar to the $\cdot O_2^-$ generating a profile, no detectable CO was treated with US, BiOCl NSs, and $BiOCl/Bi_2O_3$ NSs alone. On the basis of the excitation of US, the BiOCl NSs and $BiOCl/Bi_2O_3$ NSs began to catalyze CO_2 reduction, and $BiOCl/Bi_2O_3$ NSs exhibited efficient CO generation. Enhanced CO yields were observed under the hypoxic environment. Because of the CO_2 and O_2 reductions being undergone by the excited electrons, there was a certain amount of competition between them. Compared with CO_2 reduction, O_2 reduction was much easier, so this heterojunction catalyst preferred to catalyze the reaction under normal O_2 concentration. Hence, many more excited electrons were saved from catalyzing CO_2 reduction under a hypoxic environment. Third, dithiobisnitrobenzoicacid (DTNB) was applied as a GSH probe to assess the consumption of GSH. Negligible GSH change was shown in Fig. 3F and fig. S11 undertreated with US, the BiOCl NSs, and $BiOCl/Bi_2O_3$ NSs alone. Coupling US excitation with NSs, a noticeable GSH consumption was observed in Fig. 3F, in which $BiOCl/Bi_2O_3$ NSs + US treatment exhibited the most potent ability for GSH consumption. Fourth, methylene blue (MB) was selected as a probe to characterize the ability of ·OH generation of BiOCl NSs and $BiOCl/Bi_2O_3$ NSs. Compared with US, BiOCl NSs, and $BiOCl/Bi_2O_3$ NSs, the combination between US and NSs exhibited an evident ·OH generation (Fig. 3H and fig. S12). The highest ·OH generation was obtained using coupling $BiOCl/Bi_2O_3$ NSs with US excitation.

The band structure, including bandgaps, CB levels, VB levels, and the electrostatic potentials, including work functions and Fermi levels, were calculated to deeply dip the $BiOCl/Bi_2O_3$ NS–mediated multimodel catalytic therapy under US irradiation. First, the band structure of prepared NSs was calculated through diffuse reflection absorption and XPS spectra. As shown in Fig. 4A and fig. S13, two curves resulted from the heterogeneous structure of $BiOCl/Bi_2O_3$ NSs, and the bandgaps (E_g) of BiOCl and Bi_2O_3 in $BiOCl/Bi_2O_3$ NSs were 3.5 and 2.8 eV, respectively. The VB values of BiOCl and Bi_2O_3 in $BiOCl/Bi_2O_3$ NSs were 2.4 and 3.2 eV, respectively, developed from the XPS spectra (Fig. 4B). Next, on the basis of the difference between E_g and VB, the CB values of BiOCl and Bi_2O_3 were evaluated to be −1.1 and 0.4 eV, respectively.

In practice, defects are inevitable, playing an essential role in the properties of crystals (*44*, *45*). Using vacancy formation energy, we further considered the difficulty of forming point defects in BiOCl and Bi_2O_3. Figure 4C illustrates the formation energies of all possible point vacancies in BiOCl and Bi_2O_3. In BiOCl, only one type of Bi, O, and Cl monovacancy could be formed, and the corresponding formation energies were 10.92, 7.29, and 4.68 eV, respectively. At the same time, there were two and three types of Bi and O monovacancy in Bi_2O_3, with the formation energies ranging from 6.39 to 10.19 eV. Cl@BiOCl had the lowest formation energy, meaning that Cl vacancy was most likely to appear in the $BiOCl/Bi_2O_3$ heterojunction. Work function is an essential parameter reflecting the field-emission properties of materials. Density functional theory (DFT), therefore, understands the work function of pristine BiOCl, Cl-defective BiOCl, and pristine Bi_2O_3. Figure 4D shows the planar-averaged electrostatic potentials of all the considered systems. Moreover, the vacuum and Fermi levels were marked using blue and red lines, respectively. Compared with the BiOCl NSs, the Bi_2O_3 NSs had a lower vacuum level but a significantly higher Fermi level. The work function of BiOCl and Bi_2O_3 was found to be 6.68 and 4.81 eV, respectively. However, the phenomenon was reversed after Cl vacancy was introduced into BiOCl. The Fermi level of BiOCl was elevated higher than Bi_2O_3 (the vacuum energy level was taken as 0 eV) by the Cl vacancy, resulting in a lower work function, and electrons could quickly form BiOCl. When Cl-defective BiOCl was in contact with Bi_2O_3, electrons migrated spontaneously from BiOCl to Bi_2O_3 until the Fermi level reached the same, resulting in a built-in electric field, which is the key to Z-scheme electron transmission. The BiOCl is positively charged at the interface, while the Bi_2O_3 is negatively charged. This result was consistent with the charge transfer from BiOCl to Bi_2O_3, as revealed by XPS results. As displayed in Fig. 2, Fe 2p, Cl 2p, and O 1s in $BiOCl/Bi_2O_3$ NSs were shifted from 0.2 to 0.5 eV toward higher binding energy compared with those of pristine BiOCl NSs. The results demonstrated that the electrons transferred from BiOCl to Bi_2O_3 upon hybridization due to the difference in their work functions and Fermi levels. Such electron transfer also showed that a built-in electric field was constructed within the interfaces that connected BiOCl to Bi_2O_3. Moreover, it facilitated the construction of Z-scheme $BiOCl/Bi_2O_3$ heterojunction without any redox mediator, efficiently separating the charge carriers and thus promoting the reduction and oxidation reactions catalyzed by separated electrons and holes. The built-in electric field–facilitated Z-scheme charge transfer in the $BiOCl/Bi_2O_3$-based heterojunction was presented in Fig. 4E. US irradiation excited the electron-hole pair separation in the VB of BiOCl and Bi_2O_3 synchronously, in which the excited electrons transition across the bandgap to the catalyst CB, while the holes remain in the VB. Then, under the guidance of built-in electric field, the electrons in the CB of Bi_2O_3 were recombined with the holes in the VB of BiOCl, leaving more substantial reduction/oxidation potentials within the CB of BiOCl and the VB of Bi_2O_3. Moreover, the E^0 of oxidation of $H_2O/\cdot OH$ (2.73 eV) and GSH/GSSG (0.3 eV) was lower than that of the VB of Bi_2O_3, respectively. The E^0 reduction of $O_2/\cdot O_2^-$ (−0.28 eV) and CO_2/CO (−0.53 eV) was lower than that of the CB of BiOCl.

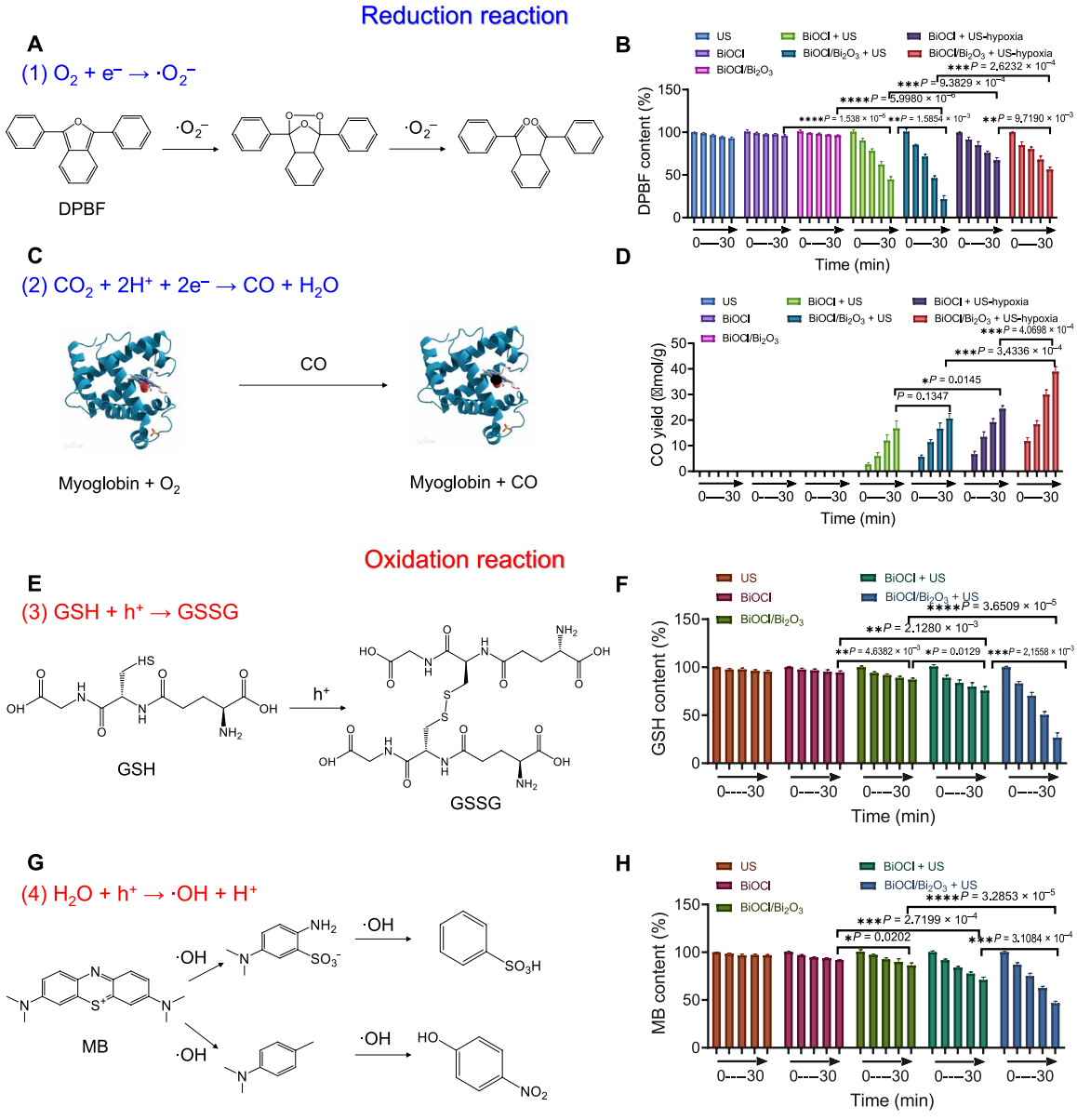

Fig. 3. Catalytic performance and mechanism of BiOCl NSs and BiOCl/Bi_2O_3 NSs. The mechanism (**A**) and performance (**B**) of $\cdot O_2^-$ generation with US-excited electrons. The mechanism (**C**) and performance (**D**) of CO generation with US-excited electrons. The mechanism (**E**) and performance (**F**) of GSH consumption with US-excited holes. The mechanism (**G**) and performance (**H**) of ·OH generation with US-excited holes.

Therefore, on the basis of US irradiation, it is feasible and convenient for H_2O oxidation to produce ·OH and GSH oxidation through the holes in the VB of Bi_2O_3 and the reducing O_2 and CO_2 to produce $\cdot O_2^-$ and CO (Fig. 4E). Although the sites of catalytic oxidation reactions (GSH → GSSG and H_2O → ·OH) were located on Bi_2O_3, it does not mean that the occurrence and efficiency of the two oxidation reactions attribute to Bi_2O_3 alone. The extended lifetime of the excited electrons and holes due to unique Z-schemed electron transport should be the primary reason for efficient catalytic water splitting and GSH oxidation. To further confirm the superiority of Z-scheme BiOCl/Bi_2O_3 heterojunction, the ·OH production, and GSH oxidation were investigated using Bi_2O_3 alone as a catalyst based on US irradiation. As shown in fig. S15, without the support of 2D nanostructure and Z-scheme heterojunction, Bi_2O_3-based nanocatalyst has very low efficiency in catalyzing GSH oxidation and ·OH generation. It cannot effectively induce tumor cell apoptosis. Although the BiOCl/Bi_2O_3 NS–based heterojunction has two active centers for catalytic oxidation and reduction, the degree of its catalytic reverse reaction, such as oxidation reactions ($\cdot O_2^-/O_2$ and CO/CO_2) or reduction reactions (GSSG/GSH and $\cdot OH/H_2O$), should be very low. There are two main reasons: First, in the TME, compared with O_2, CO_2, GSH, andH_2O, the contents of their redox products such as $\cdot O_2^-$, CO, GSSG, and ·OH are much lower. According to the catalytic reaction equilibrium theory, the catalyst preferentially catalyzes the high concentration substrate, so the reversible reaction proceeds in a positive direction as a whole. In addition, ROS, including $\cdot O_2^-$, ·OH, and CO, all have a very short lifetime, which will immediately oxidize and damage the surrounding

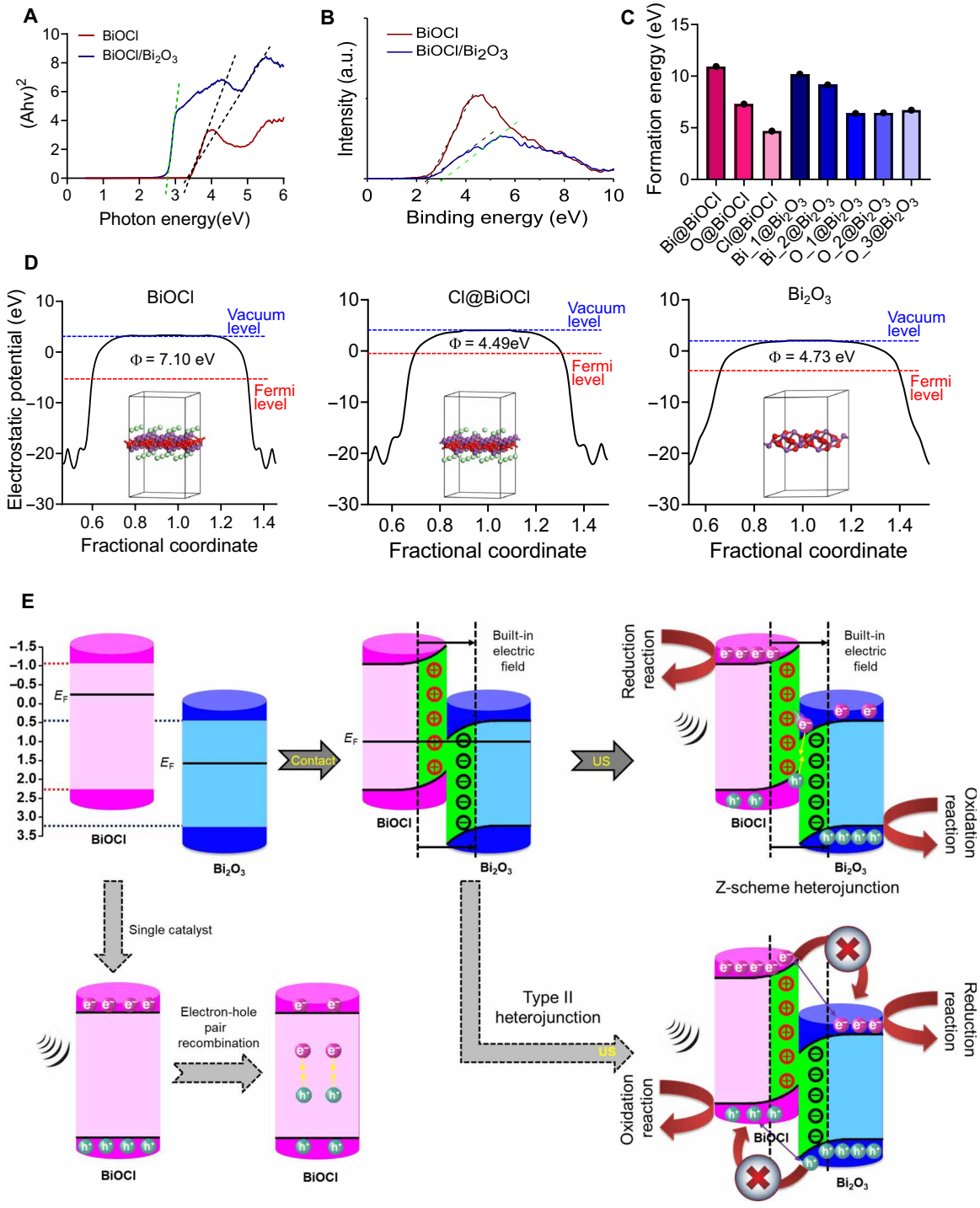

Fig. 4. Analysis of the catalytic mechanism of BiOCl/Bi_2O_3 NSs. (**A**) Bandgaps and (**B**) the valance band of BiOCl NSs and BiOCl/Bi_2O_3 NSs. (**C**) The formation energy of different vacancies of BiOCl NSs and BiOCl/Bi_2O_3 NSs. (**D**) The DFT computationally calculates BiOCl, Cl@BiOCl, and Bi_2O_3. (**E**) Mechanism of the Z-schemed heterojunction based on BiOCl/Bi_2O_3 NSs.

tumor cell membrane, organelles, DNA, etc. and quickly consume up. Therefore, the reaction will continue in the positive direction based on equilibrium theory of reversible catalytic reaction.

The adsorption of reactant and catalyst is the first step within a catalytic reaction and determines the possibility and efficiency of the reaction. We estimated the adsorption behavior for each reactant on the corresponding catalyst in this study. The initial distance between the reactant and catalysis was set to be 3.0 Å, and all possible molecular orientations and conformations were evaluated. We analyzed the density of states of pristine Bi_2O_3- and Cl-defective BiOCl to determine the initial adsorption sites, respectively. As illustrated in fig. S14, the VB maximum of Cl-defective BiOCl has

Bi characters, indicating that Bi atoms participate in the reduction reactions. In contrast, O characters contribute to the CB minimum of pristine Bi_2O_3. Thus, the oxidation reactions will occur around the O atoms of Bi_2O_3. There are three types of O atoms present in the Bi_2O_3 primitive cell; the Wyckoff position for the O atoms are O1 (0.44, 0.40, 0.50), O2 (0.42, 0.64, 0.45), and O3 (0.25, 0.37, 0.51). The favorite adsorption energies of H_2O molecules at the three binding sites were calculated to be −0.70, −0.88, and −0.71 eV. Therefore, position O_2 was the most favorable site for oxidizing H_2O molecules. The results were consistent with the prediction of hydrophilic properties, establishing that the self-consistent methodology in this work could become self-consistent. After adsorbing to Bi_2O_3, the length of the O—H bond near the adsorption surface was elevated to 1.021 Å. The charge density difference profiles for isolated and adsorbed H_2O reveal the bonding mechanisms. As shown in Fig. 5A, the electron cloud between the O atom and the H atom in the H_2O molecule close to Bi_2O_3 is reduced significantly. Thus, adsorption causes the H_2O molecule to dissociate more efficiently, and ·OH is generated. For adsorbing GSH on Bi_2O_3, the most favorite adsorption configuration with −3.54 eV is shown in Fig. 5B. The conformation of GSH underwent some adjustments, mainly reflected in the rotation of the sulfhydryl group toward the surface of the Bi_2O_3 NS to achieve a stable adsorption state. The bond length of the H—S bond in adsorbed GSH was 0.02 Å longer than the isolated one. The adsorption energy of the GSH-Bi_2O_3 complex was calculated to be −3.54 eV, indicating that the GSH molecule was chemisorbed on the NS. This is due to the three hydrogen bonds and one O—Bi bond that formed between GSH and Bi_2O_3.

Among them, the hydrogen bond formed between the sulfhydryl group and Bi_2O_3 makes the O atom near the sulfhydryl group accepts 0.76 electrons from the GSH molecule. The results indicated that chemical adsorption made the GSH molecule anchors the sulfhydryl group on the Bi_2O_3 NS, reducing its consumption of the ROS molecules. In addition, the adsorption process also provides a prerequisite for Bi_2O_3 to catalyze GSH and generate GSSG, conducive to ROS accumulation within the TME. For the O_2 adsorption system, the Bader charge analysis was used to obtain the specific charges of the O_2 molecule and BiOCl. As shown in Fig. 5C, the electrons flowed from the BiOCl to O_2 during the adsorption process. Furthermore, the obtained adsorption energy is −0.06 eV, allowing the O_2 molecule to escape after accepting electrons from BiOCl. Dissociative adsorption of CO_2 after being exposed to Cl-defective BiOCl is displayed in Fig. 5D: One of the C—O bonds breaks, and the dissociated O atom forms a chemical bond with two Bi atoms of BiOCl. Meanwhile, one CO molecule is physisorbed on the BiOCl NS through the van der Waals force. The results further support the catalytic activity for CO_2 reduction on the BiOCl NSs.

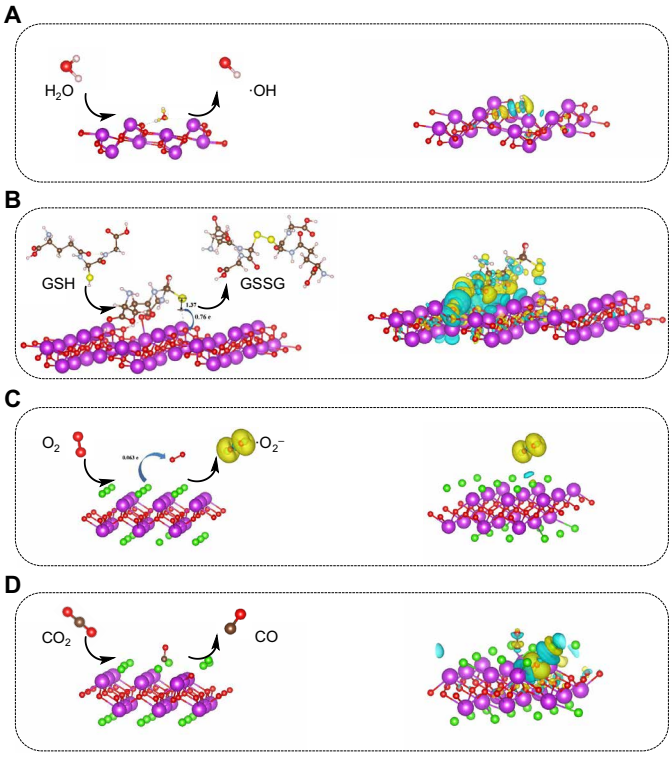

Fig. 5. Favorite adsorption configuration, catalytic mechanism, and the charge density difference of substrates adsorbed on the catalyst. (**A**) Bi_2O_3 catalyzes H_2O oxidation, (**B**) Bi_2O_3 catalyzes GSH oxidation, (**C**) BiOCl catalyzes O_2 reduction, and (**D**) BiOCl catalyzes CO_2 reduction.

Antitumor strategy and biocompatibility in vitro

Next, the in vitro catalytic performance and the antitumor effect of BiOCl NSs and BiOCl/Bi_2O_3 NSs were investigated. The biocompatibility of BiOCl NSs and BiOCl/Bi_2O_3 NSs with normal cells, including human embryonic kidney cells (HEK293), normal human liver cells (HL-7702), and normal human mammary epithelial cells (MCF-10A) were detected through the 3-(4,5-dimethyl-2-thiazolyl)-2,5-diphenyl-2-H-tetrazolium bromide (MTT) assay. Moreover, the cytotoxicity of BiOCl NSs and BiOCl/Bi_2O_3 NSs with or without PEGylation was determined to confirm the function of PEGylation. As shown in Fig. 6A and fig. S16, the BiOCl/Bi_2O_3 NSs exhibited concentration-dependent cytotoxicity against the detected normal human cells before PEGylation. However, BiOCl NSs and BiOCl/Bi_2O_3 NSs exhibited good biocompatibility and safety toward normal cells after PEGylation, demonstrating the notable role of PEGylation in nanomedicine. Next, specific cytotoxicity to cancer cells of PEGylated NSs was evaluated. In contrast, the PEGylated BiOCl/Bi_2O_3 NSs showed specific cytotoxicity toward cancer cells (Fig. 6B for HepG2 and fig. S17 for MCF-7). Two potential factors contributed to the cytotoxicity of BiOCl/Bi_2O_3 NSs: The Fenton-like reaction catalyzed by BiOCl/Bi_2O_3 NSs and GSH absorption on BiOCl/Bi_2O_3 NSs, synergistically inducing intracellular redox equilibrium disruption. The Fenton-like effect of BiOCl/Bi_2O_3 NSs with Cl defect was investigated through calculation and experiments to analyze the mechanism of the specific cytotoxicity to tumor cells. At first, to understand the behavior of overexpressed H_2O_2 in the TME after the heterojunction catalyst treatment, the "Gibbs free energy change (ΔG) of the Fenton-like reaction was determined using the following pathway

$$*+H_2O_2 \rightarrow *OH + \cdot OH \quad (a)$$

$$*OH \rightarrow * + \cdot OH \quad (b)$$

where *OH stands for the catalyst-hydroxide pair.

The free energy of the Fenton-like reaction is illustrated in fig. S18. The total energy required for a Fenton-like response is 2.31 eV, independent of the catalyst species. For Bi_2O_3 and BiOCl, one H_2O_2 molecule undergoes step (a) to generate one ·OH molecule with a

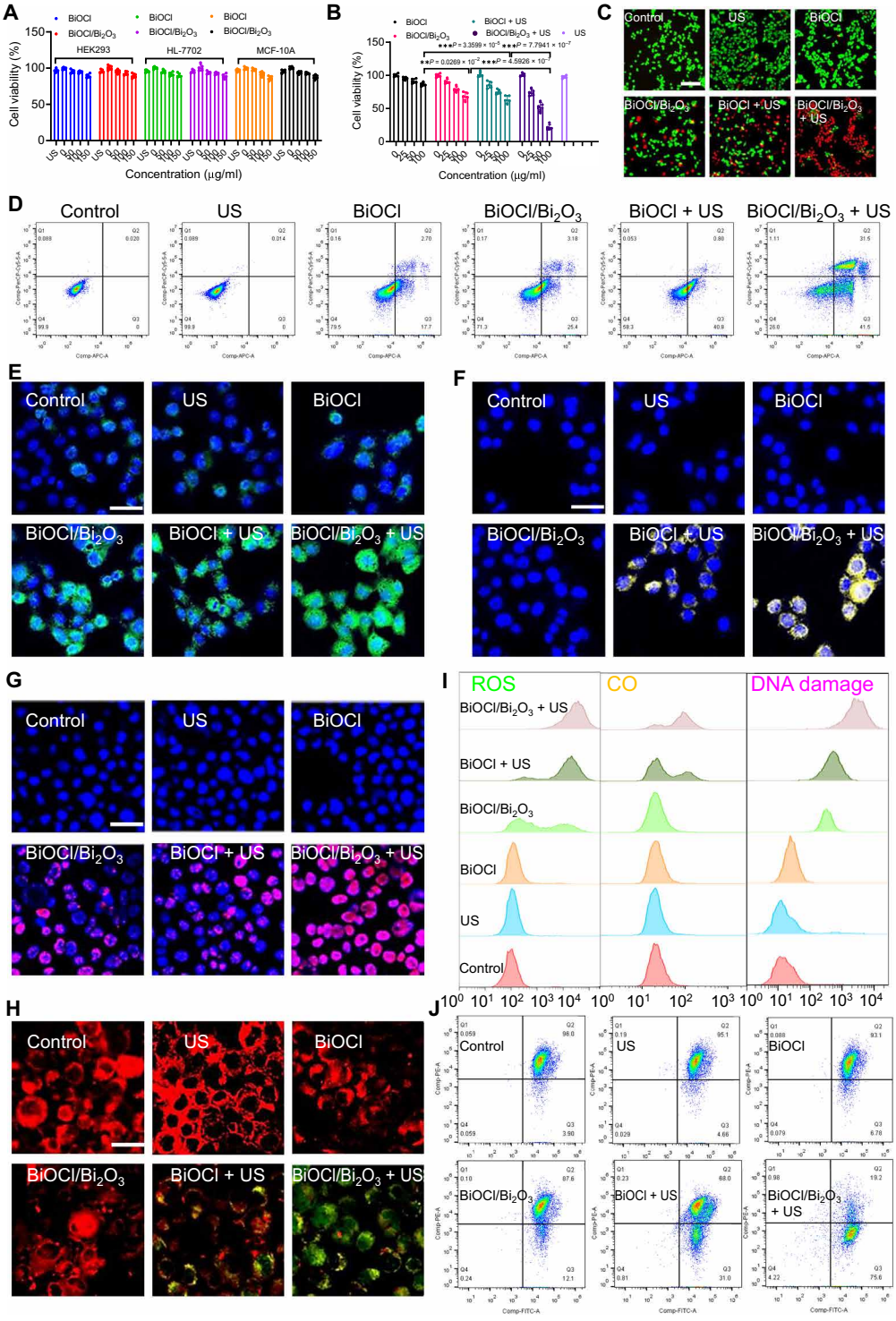

Fig. 6. The biocompatibility and cytotoxicity of BiOCl NSs and BiOCl/Bi_2O_3 NSs. (**A**) The biocompatibility of BiOCl NSs and BiOCl/Bi_2O_3 NSs for HEK293, HL-7702, and MCF-10A. (**B**) The cytotoxicity of BiOCl NSs and BiOCl/Bi_2O_3 NS–based treatments for HepG2. (**C**) The live/dead staining images of HepG2 cells under various treatments. Scale bar, 100 μm. (**D**) Apoptosis behaviors of HepG2 cells under different treatments were detected using flow cytometry. (**E**) The intracellular ROS generation, (**F**) CO generation, (**G**) early DNA damage, and (**H**) mitochondrial membrane potential change of HepG2 cells under various treatments. (**I**) The intracellular ROS generation, CO generation, early DNA damage, and (**J**) the mitochondrial membrane potential change of HepG2 cells under different treatments were detected through flow cytometry. The nuclei were stained with 4′,6-diamidino-2-phenylindole (DAPI; blue). The intracellular ROS were stained with DHE (green). The intercellular CO was stained with the FL-CO-1 CO probe (yellow). The γH2AX foci per nucleus were stained with an anti-γH2AX antibody (red). The mitochondrial membrane potential loss was stained by JC-1 (green). The live and dead cells were stained with calcein AM (green) and propidium iodide (PI) (red). Scale bars, 50 μm.

ΔG of 1.17 and 2.22 eV, respectively, and then proceeds to release one ·OH molecule with a ΔG of 1.13 and 0.08 eV. Thus, Fenton-like reactions with Bi_2O_3 and BiOCl as catalysts could be endothermic and nonspontaneous. Although the ΔG of step (b) was raised to 3.63 eV, the ΔG of the Cl-defective BiOCl catalytic system was reduced to −1.33, implying a marked reversal of the spontaneity of step (a). Therefore, we hypothesize that the Cl defect leads to the spontaneous partial Fenton-like reaction, which mediates tumor cytotoxicity. Besides, the ·OH production of prepared BiOCl/Bi_2O_3 NSs was also detected. As shown in figs. S19 and S20, there was no ·OH generation based on reactions between BiOCl or Bi_2O_3 with H_2O_2. However, a certain amount of ·OH was produced using the Fenton-like effect of BiOCl/Bi_2O_3 NSs with Cl-defective BiOCl, consistent with the computer simulation.

In addition, coupling BiOCl NSs with US irradiation, the O_2 was catalyzed to $\cdot O_2^-$. Moreover, CO_2 could be catalyzed to CO using the US-excited electrons of BiOCl NSs due to the hypoxic microenvironment. Z-scheme BiOCl/Bi_2O_3 NS–based interplanar heterojunction exposed to US irradiation exhibited the highest cytotoxicity to cancer cells. More than 85% of tumor cells were dead with BiOCl/Bi_2O_3 NSs (100 μg/ml) and 5 min of US irradiation (Fig. 6B). The leading cause of this excellent antitumor performance of BiOCl/Bi_2O_3 NSs should be attributed to the extended catalytic selectivity, including two reductions (O_2/$\cdot O_2^-$ and CO_2/CO) and two oxidation (H_2O/·OH and GSH/GSSG) reactions. The extended catalytic selectivity of BiOCl/Bi_2O_3 NSs effectively avoids the TME limitation and synergistically induces tumor apoptosis. Moreover, the cytotoxicity of different treatments to the cancer cell and their apoptosis behaviors were evaluated using fluorescent staining and flow cytometry. The live/dead fluorescent staining and flow cytometry exhibited the excellent antitumor performance of BiOCl/Bi_2O_3 NSs coupling with US irradiation (Fig. 6, C and D). Some rescue experiments were carried out, including adding GSH or vitamin (Vc) as a ROS inhibitor to verify the antitumor mechanism and the catalytic therapy of BiOCl/Bi_2O_3 NSs. As shown in fig. S21, after adding GSH and Vc, the cell viabilities were improved under the treatment of BiOCl/Bi_2O_3 NSs, BiOCl NSs + US, and BiOCl/Bi_2O_3 NSs + US, further demonstrating the excellent antitumor mechanism of BiOCl/Bi_2O_3 NSs through catalytic therapy.

Next, the properties of BiOCl/Bi_2O_3 NSs interplanar heterojunction–mediated catalytic effects were investigated on a cellular level using immunofluorescence staining inside the HepG2 cells. Figure 6 (E to H) demonstrated the immunofluorescence images of intracellular ROS content (green), CO generation (yellow), early DNA damage (pink), and mitochondrial membrane injury (green). Excessive ROS directly damages the DNA double strand in the nucleus. In contrast, excessive CO in the cell will directly change the polarization potential of the mitochondrial membrane, causing early DNA damage and mitochondrial membrane damage. Because of the high biocompatibility of BiOCl NSs, on the basis of the control and US group, BiOCl NS treatment exhibited a negligible chance of the above indicators. Because of the Fenton-like reaction catalyzed by BiOCl/Bi_2O_3 NSs and GSH absorption, the intracellular ROS content was elevated by being treated with BiOCl/Bi_2O_3 NSs, leading to evident early DNA damage. Coupling with US irradiation, BiOCl NSs could catalyze O_2 reduction and a small amount of CO_2 reduction, generating $\cdot O_2^-$ and CO (Fig. 6, E and F). Subsequently, the early DNA damage and polarization potential of the mitochondrial membrane responded accordingly in Fig. 6G within 6 hours. For BiOCl/Bi_2O_3 NSs + US treatment, large amounts of ROS and CO contents were observed in Fig. 6 (E and F) due to the omnipotent and synergistic catalytic effects, leading to extensive DNA and mitochondrial membrane damages. Moreover, the intracellular ROS and CO generation, early DNA damage, and mitochondrial membrane potential change were further analyzed by flow cytometry (Fig. 6, I to J), which further demonstrated the specific and efficient antitumor performance based on BiOCl/Bi_2O_3 NSs coupling with US irradiation. For the flow cytometry analysis of mitochondrial membrane potential change under different treatments (Fig. 6J), the treatments of US and BiOCl NSs did not change the membrane potential of cancer cells, and 5,5′,6,6′-Tetrachloro-1,1′,3,3′-tetraethyl-imidacarbocyanine (JC-1) enters the mitochondria through the polarity of the mitochondrial membrane and forms a polymer emitting red fluorescence due to the increase in concentration. Because of the generation of ROS treated by BiOCl/Bi_2O_3 NSs inducing apoptosis, the mitochondrial transmembrane potential depolarizes, JC-1 is released from the mitochondria, and the concentration decreases, reversing to the monomer form emitting green fluorescence. Moreover, BiOCl/Bi_2O_3 NSs + US treatment mediated much more cell apoptosis, which emitted more green fluorescence. Therefore, changes in mitochondrial membrane potential can be detected qualitatively (shift of cell population) and quantitatively (fluorescence intensity of cell population) by detecting green and red fluorescence.

Biodistribution and antitumor strategy in vivo

The in vivo therapeutic performances of BiOCl/Bi_2O_3 NSs were investigated. At first, the biodistribution of BiOCl/Bi_2O_3 NSs was determined through intravenous injection of Cy5.5-loaded BiOCl/Bi_2O_3 NSs to the HepG2 xenograft tumor model. Figure 7A demonstrated the biodistribution of BiOCl/Bi_2O_3 NSs. Figure 7B showed the fluorescent images of the major organs and tumor after 24 hours after injection, indicating a specific accumulation of nanoscale BiOCl/Bi_2O_3 NSs at the tumor site due to enhanced permeability and retention effect *(46–48)*. In addition to fluorescence imaging, BiOCl/Bi_2O_3 NSs could also be computed tomography (CT) imaging agents based on the high x-ray attenuation coefficient of Bi. As shown in Fig. 7 (C and D), BiOCl/Bi_2O_3 NSs have a good linear relationship between concentration and the Hounsfield units (HU) value. Then, the in vivo CT imaging potential of BiOCl/Bi_2O_3 NSs was investigated by intravenously injecting them into HepG2 tumor–bearing mice. As observed in Fig. 7E, the results showed that enhanced contrast was discerned in the HepG2 tumor from coronal CT images, with HU values increasing from 7.0 to 93.2, at 24 hours following intravenous injection of BiOCl/Bi_2O_3 NSs into HepG2 tumor–bearing nude mice. Therefore, BiOCl/Bi_2O_3 NSs could be an efficient CT imaging agent during in vivo cancer diagnosis. Pharmacokinetic analysis (fig. S22) depicted the long circulation time of BiOCl/Bi_2O_3 NSs. In addition, an inductively coupled plasma (ICP) emission spectrometer was applied to precisely analyze the in vivo biodistribution of BiOCl/Bi_2O_3 NSs. As shown in fig. S23, the concentration of NSs inside the major organs and tumors over 24 hours was exhibited, in which an excellent tumor accumulation of the prepared NSs was also depicted. However, the biodistribution of BiOCl/Bi_2O_3 NSs, especially in the tumor, is inconsistent between fluorescent imaging and ICP. The degradation of Cy5.5 catalyzed by BiOCl/Bi_2O_3 NSs mediated the Fenton-like effect in the entire TME (fig. S24).

The in vivo therapeutic performance of BiOCl NSs and BiOCl/Bi_2O_3 NSs was carried out considering the high tumor accumulation.

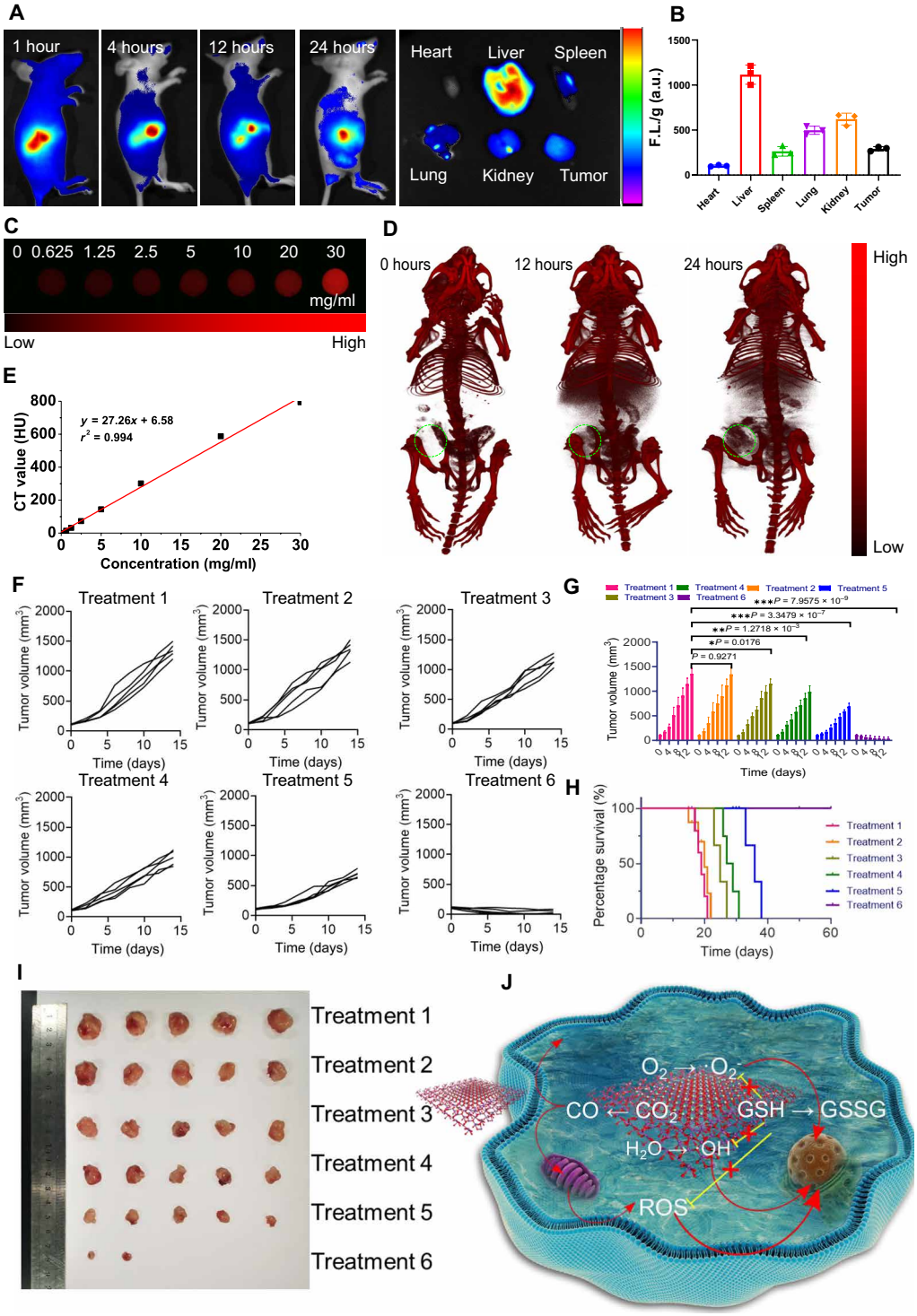

Fig. 7. In vivo imaging, biodistribution, and antitumor study of the BiOCl/Bi_2O_3 NSs. (**A**) In vivo fluorescence images of nude mice at different time points after intravenous injection using Cy5.5-labeled NSs and ex vivo fluorescence images of tumor and major organs at 24 hours after injection. (**B**) Semiquantitative biodistribution of Cy5.5-labeled NSs in nude mice was detected using the average fluorescence intensity of tumors and the major organs per gram. F.L., Fluorescein. (**C**) The CT images of BiOCl/Bi_2O_3 NSs with different concentrations. (**D**) The CT values (HU) of BiOCl/Bi_2O_3 NSs. (**E**) Time-dependent whole-body CT imaging of the tumor-bearing mouse after intravenous injection of NSs. The green circle indicates a tumor. (**F** and **G**) Tumor growth curves under different treatments. (**H**) Mouse survival curves under various treatments. (**I**) Tumor images after 14 days of various treatments. (**J**) The cure mechanism of BiOCl/Bi_2O_3 NSs through US irradiation.

HepG2 tumor–bearing mice were randomly separated into six groups and received different treatments: treatment 1, saline; treatment 2, US; treatment 3, BiOCl NSs; treatment 4, BiOCl/Bi_2O_3 NSs; treatment 5, BiOCl NSs + US; and treatment 6, BiOCl/Bi_2O_3 NSs + US. The BiOCl NS and BiOCl/Bi_2O_3 NS dose intravenously injected into mice in treatments 3, 4, 5, and 6 was 4 mg/kg. The US treatment (1 MHz, 0.8 W cm^{-2}, 50% duty cycle) in treatments 5 and 6 were performed 24 hours after injection of NSs (fig. S25). As shown in Fig. 7 (F and G), no significant tumor growth inhibition was observed in control (treatment 1), US only (treatment 2), and BiOCl NSs (treatment 3). However, to a certain extent, tumor growth inhibition was exhibited in BiOCl/Bi_2O_3 NSs alone treated mice (treatment 4). It was attributed to the Fenton-like reaction and absorption of GSH by BiOCl/Bi_2O_3 NSs, inducing intracellular REDOX imbalance. Treatment 5 provided a better therapeutic effect than treatment 3, indicating the advantages of US irradiation for triggering O_2 and CO_2 reduction. Treatment 6 demonstrated extreme inhabitation of tumor growth due to the omnipotent and synergistic catalytic effects through BiOCl/Bi_2O_3 NS–based interplanar heterojunction with expansive catalytic selectivity. Therefore, the tumors treated with BiOCl/Bi_2O_3 NSs coupling with US irradiation were nearly eliminated. The dissected tumors (Fig. 7I) provided direct evidence for the therapeutic outcomes of interplanar heterojunction–mediated catalytic therapy. Correspondingly, the BiOCl/Bi_2O_3 NSs coupled with US treatment were associated with a significantly high survival rate (Fig. 7H). In addition, no noticeable side effects were observed based on different treatments (fig. S26).

Antitumor mechanism and biocompatibility analysis in vivo

To further confirm the specific targeted antitumor mechanism and biocompatibility of BiOCl/Bi_2O_3 NS–based catalytic therapy, the histological analyses through the hematoxylin and eosin (H&E) staining, CO contents through Spiro[isobenzo furan-1(3H),9′-[9H] xanthen]-3-one (COP-1), DNA damage levels through γ-H2AX staining, and apoptosis levels using cleaved caspase-3 (C-CAS3) staining were undergone in vivo. As depicted in Fig. 8, although partially intravenously injected BiOCl/Bi_2O_3 NSs were accumulated within other organs and nearly no CO generation, DNA damage, cell apoptosis, and the destruction of normal organs (including heart, liver, spleen, lung, and kidney) were demonstrated without direct US irradiation. In the histological analyses of the H&E staining image of the tumor, there was extensive destruction of the tumor tissue (Fig. 8A). As shown in Fig. 8B, a large amount of CO was produced through BiOCl/Bi_2O_3 NSs coupling with US irradiation. Moreover, many DNA damages and apoptosis of cancer cells were observed using the immunofluorescence staining images of tumors treated with BiOCl/Bi_2O_3 NSs + US (Fig. 8C). The current in vivo analysis further established that the intrinsic interplanar heterojunction of BiOCl/Bi_2O_3 NS–based catalytic therapy mediated an efficient, targeted cancer therapy by improving the REDOX potential energy and extending substrate selectivity. Moreover, it also guarantees an excellent biosafety for normal organs.

Considering that the in vivo toxicity of the materials has an essential role in translation from bench to practical applications, we set forth to evaluate the toxicity of BiOCl/Bi_2O_3 NSs. Immune analysis, histology examination, and hematology assay were additionally detected. Blood examination was carried out at 1, 7, and 14 days after intravenous injection of BiOCl/Bi_2O_3 NSs for the histology and hematology assay. As shown in fig. S27, no statistically significant differences in the levels of aspartate aminotransferase (AST), lactate dehydrogenase, alkaline phosphatase, alanine aminotransferase (ALT), or blood urea nitrogen (BUN) were detected in mice receiving BiOCl/Bi_2O_3 NSs than the control mice. For immune analysis, the amount of interleukin 6 (IL-6), interferon-γ (IFN-γ), tumor necrosis factor–α (TNF-α), and IL-12 + P40 were measured in serum samples from mice at 2 and 24 hours after intravenous injection of BiOCl/Bi_2O_3 NSs. As exhibited in fig. S28, the cytokine levels from the BiOCl/Bi_2O_3 NS–treated group revealed no noticeable difference compared with the control group. It also established that the prepared BiOCl/Bi_2O_3 NSs showed good biocompatibility and biosafety in vivo.

DISCUSSION

Chemotherapy is the primary choice for most cancer patients due to its broad spectrum and reliable curative effect. However, the clinical use of small-molecule chemotherapy drugs depicts some problems, including poor selectivity, low bioavailability, and obvious toxic side effects *(49–52)*. Catalytic therapy converts the substrate within the TME into effective therapeutic drugs by addressing the specific internal microenvironment or exogenous stimulation of the tumor site. Moreover, it uses the in situ catalytic reaction in the tumor initiated by nontoxic or low toxic nanocatalysts to achieve tumor cell–specific oxidative damage and cell death without obviously affecting the normal tissue (*7*). However, the clinical application of catalytic therapy has the following two problems: (i) The traditional nanocatalysts have weak catalytic power due to the fast recombination rate of excited electrons and holes; (ii) the types and concentrations of substrates catalyzing in the microenvironment are minimal, leading to low catalytic efficiency.

Our work creates an interplanar heterojunction based on 2D BiOCl/Bi_2O_3 NSs capable of prolonging the life span of electrons and holes and extending substrate selectivity. Moreover, its proof-of-concept application becomes a new heterojunction-based catalytic therapy platform for effective cancer therapy. First, an intelligent edge modification was developed to integrate interplanar heterojunction synthesis and exfoliate the ultrathin NSs. After PEGylation, the engineering BiOCl/Bi_2O_3 NSs functionalized through a characteristic interplanar heterojunction to efficiently catalyze O_2 and CO_2 reduction and H_2O and GSH oxidation under US irradiation. In the interplanar heterojunction BiOCl/Bi_2O_3 NSs, BiOCl and Bi_2O_3 parts with different Fermi levels and energy band structures contacting each other induce charges to redistribute at their interfaces by the aligning Fermi levels. Thus, it mediates the construction of a built-in electric field in its interface. Under US irradiation, the US-excited electrons at the CB of Bi_2O_3 were combined with the holes at the VB of BiOCl guided by the built-in electric field at their interface, leaving more substantial reduction/oxidation potentials of separated electrons and holes at the CB of BiOCl and the VB of Bi_2O_3. Meanwhile, a Schottky barrier was formed because of band bending at their interface, preventing the electron flow from BiOCl to Bi_2O_3 and enhancing their Z-schemed charge transfer. Hence, a built-in electric field and Schottky barrier facilitated a Z-schemed catalytic mechanism. The holes on the VB of Bi_2O_3 with high oxidation potential had a remarkable ability to oxidize H_2O and GSH, generating ·OH and GSSG. Meanwhile, the electrons on the CB of BiOCl with high reduction potential showed a notable ability to reduce O_2 and CO_2, developing $\cdot O_2^-$ and CO. The obtained BiOCl/Bi_2O_3 NSs

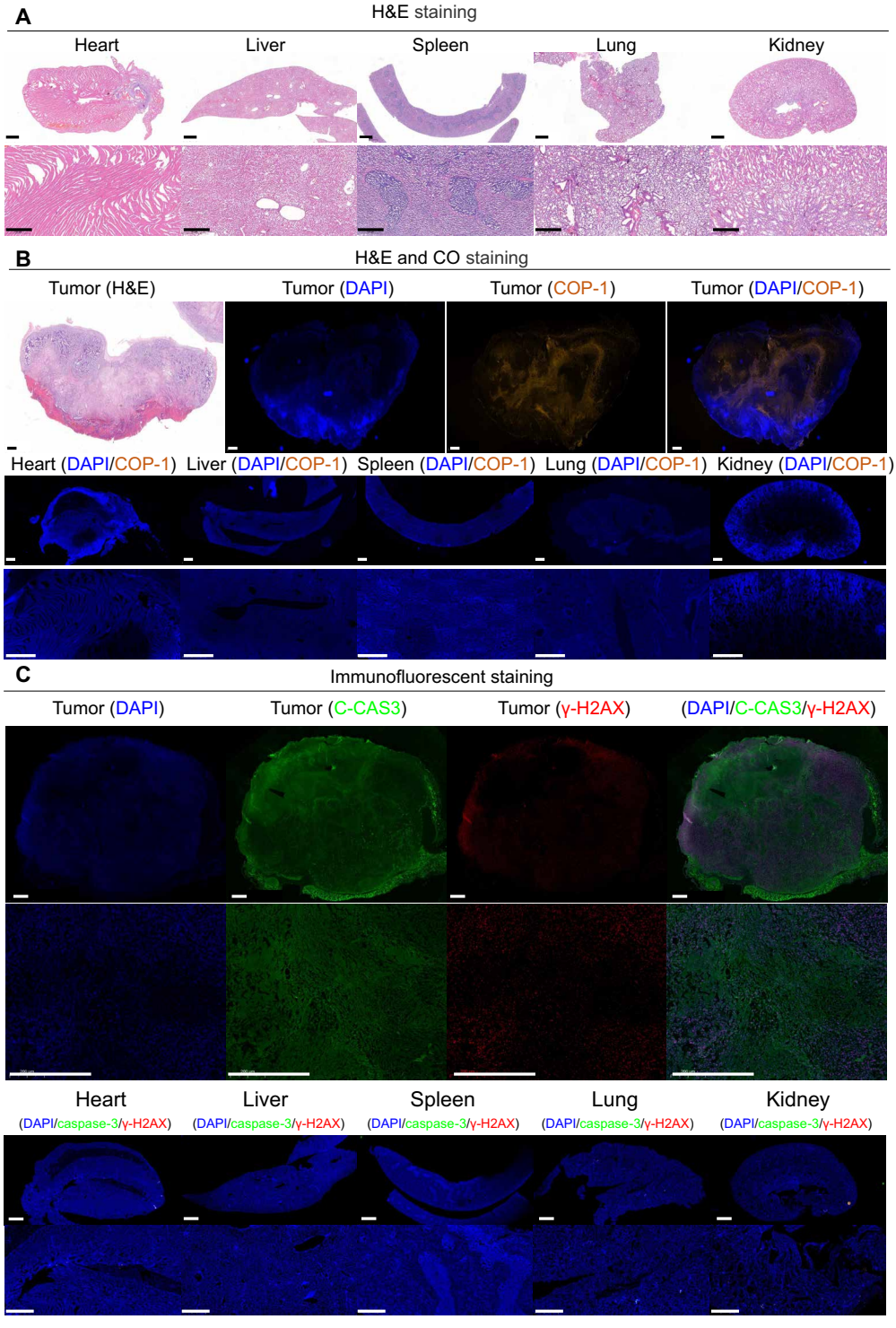

Fig. 8. $BiOCl/Bi_2O_3$ NSs based on specific targeted therapy and biocompatibility. (**A**) H&E staining images. Scale bars, 500 μm. (**B**) CO staining images and (**C**) immunofluorescent images of the major organs and tumors obtained from mice through $BiOCl/Bi_2O_3$ NSs + US treatment. Scale bars, 500 μm. The apoptotic cells were stained using the apoptosis marker C-CAS3 (green), the damaged DNA was stained with γH2AX foci (red), the generated CO was stained with COP-1 (orange), and the nucleus was stained with DAPI (blue).

with highly efficient catalytic effects exhibited excellent anticancer performance both in vitro and in vivo.

The overall objective of this study was to understand whether a 2D interplanar heterojunction platform could prolong the life span of electrons and holes, extend substrate selectivity, and promote tumor catalytic therapy. As a test case, we selected HepG2 subcutaneous transplanted tumor as the tumor model. The data showed that BiOCl/Bi_2O_3 NS–based interplanar heterojunction successfully catalyzed the O_2 and CO_2 reduction and H_2O and GSH oxidation under US irradiation in vitro and HepG2 subcutaneous transplanted tumors. Therefore, this study not only defines an excellent strategy for intelligent synthesizing 2D ultrathin interplanar heterojunction. It also solves the fundamental problem that limits the efficiency of catalytic therapy, providing a specific incentive to make valuable contributions in other possible fields in the future. In addition, more robust formulation strategies could be required to scale up and manufacture such interplanar heterojunction. More fundamental research on in vivo applications, such as long-term biosafety of catalysts, in situ tumor model experiments, etc., needs further consideration. Moreover, the findings could shed light on applying 2D interplanar heterojunction–mediated catalytic therapy against superficial diseases, such as wound antibacterial and anti-infection.

MATERIALS AND METHODS

Materials

Bismuth nitrate pentahydrate [$Bi(NO_3)_3{\cdot}5H_2O$], sodium chloride (NaCl), potassium borohydride (KBH_4), hydrogen dioxide (H_2O_2), 2,7-dichlorodihydrofluorescein diacetate, MB, GSH, $[Ru(dpp)_3]Cl_2$, and DTNB were obtained from Sigma-Aldrich. PEG-NH_2 [molecular weight (MW), 5000] and Cy5.5-PEG-NH_2 (MW, 5000) were provided by Nanocs Inc. Trypsin-EDTA, Dulbecco's minimum essential medium, RPMI 1640 medium, fetal bovine serum, and PBS (pH 7.4) were provided by Gibco Life Technologies. Alexa Fluor 647 mouse anti-H2AX (pS139) and anti-cleaved poly(adenosine 5′-diphosphate–ribose) polymerase (Asp^{214}) antibodies were secured from BD Pharmingen. Normal human liver cells (HL-7702; catalog no. 77402), human embryonic kidney cells (HEK293, catalog no. CRL-1573), normal human mammary epithelial cells (MCF-10A, catalog no. CRL-10781), human breast cancer cell (MCF-7, catalog no. HTB-22), and human hepatoma cells (HepG2, catalog no. HB-8065) were supplied by the American Type Culture Collection (ATCC). ATCC used morphology, karyotyping, and polymerase chain reaction–based approaches to confirm the identity of human cell lines and rule out intra- and interspecies contamination. Also, the cell line was frequently evaluated through its morphological features.

Preparation of BiOCl NSs and BiOCl/Bi_2O_3 NSs

First, 0.058-g NaCl was dissolved in 15 ml of distilled water containing 0.486-g $Bi(NO_3)_3 \cdot 5H_2O$ under vigorous stirring for 30 min. Second, the suspension was transferred into a 50-ml Teflon-lined stainless-steel autoclave and then heated at 170°C for 16 hours. Last, the products were washed with distilled water and ethanol and dried at 80°C for 24 hours. Later, the obtained powder was under probe sonication–assisted liquid exfoliation in water for 12 hours. After exfoliation, the unexfoliated BiOCl was removed through centrifugation at 3000 rpm for 5 min. Afterward, the supernatant was centrifuged at 12,000 rpm for 5 min, and the prepared BiOCl NSs were stored at 4°C.

For BiOCl/Bi_2O_3 NS preparation, Bi_2O_3 deposition was performed through in situ reductions and oxidation of BiOCl powder in KBH_4 and H_2O_2 solutions. BiOCl powder (0.5 g) was added to 40-ml KBH_4 solution and reacted for 10 min. The products were washed using deionized water several times to remove the chemical remnants. Then, the resulting products were added to a 40-ml H_2O_2 aqueous solution with an H_2O_2 concentration of 15% and reacted for 10 min. The resulting precipitate was washed using deionized water several times to remove the chemical remnants. The final BiOCl/Bi_2O_3 composite was within probe sonication–assisted liquid exfoliation in water for 12 hours. After exfoliation, the unexfoliated BiOCl/Bi_2O_3 was removed through centrifugation at 3000 rpm for 5 min. Afterward, the supernatant was centrifuged at 12,000 rpm for 5 min, and the as-prepared BiOCl/Bi_2O_3 NSs were stored at 4°C.

PEGylation of BiOCl NSs and BiOCl/Bi_2O_3 NSs

NSs were modified with PEG(5k)-NH_2 to improve the stability and biocompatibility of BiOCl NSs and BiOCl/Bi_2O_3 NSs. First, PEG(5k)-NH_2 (10 mg) was added to NS suspension, and then the suspension was ultrasonicated and stirred for 30 min and 12 hours, respectively. The mixture was washed thrice by centrifugation at 2500 rpm (4°C) for 30 min to remove the unattached PEG(5k)-NH_2. Afterward, the PEGylated NSs were resuspended in PBS and stored at 4°C for future use.

Characterization

SEM (JSM-6700F, JEOL, Japan), TEM (JEM-2100UHR, JEOL, Japan), and atomic force microscopy (AFM; FastScan Bio, Germany) were used to analyze the microstructure and morphology of prepared BiOCl NSs and BiOCl/Bi_2O_3 NSs. Moreover, XPS (ESCALAB 250Xi, Japan) and Fourier transform infrared spectrophotometry (Nexus 470, Nicolet, Madison, WI, USA) analyzed the chemical composition. XRD spectra, Raman shift spectra, and EDS (INCA X-MAX, Oxford, UK) evaluated the elementary composition and chemical structures of NSs. At room temperature, ultraviolet-visible (UV-vis)–near-infrared spectra of NSs were recorded using an Infinite M200 PRO spectrophotometer.

Modeling and calculation details

We used the VASP code to perform the whole spin-polarized DFT calculations. The convergence threshold was set to be 1×10^{-5} Ha in energy and 0.01 Ha/Å in force. The Perdew-Burke-Ernzerhof formalism of the generalized gradient approximation dealt with the electron exchange–correlation term. The cutoff energy was set to be 500 eV for the plane-wave expansion. The projector augmented wave approach was adopted to handle the electron-ion interactions. The DFT-D2 method of Grimme was considered the van der Waals interactions. The $3 \times 3 \times 1$ and $2 \times 2 \times 1$ supercells of BiOCl and Bi_2O_3 were repeated periodically in the *x*-*y* plane. A vacuum region of 15 Å was added to eliminate interlayer interference. The Brillouin zone integration was sampled through $4 \times 4 \times 1$ and $4 \times 5 \times 1$ Monkhorst-Pack *k*-points meshes for BiOCl and Bi_2O_3, respectively.

The adsorption of H_2O on BiOCl and Bi_2O_3 was studied more than the hydrophilic properties of the two materials. The initial binding sites for H_2O were searched through Monte Carlo annealing simulations, which allowed a rotatable molecule to randomly translate on the surface of the substrate until the local energy minima were reached.

The following equation calculated the vacancy formation energies of defective BiOCl and Bi_2O_3

$$E_{formation} = E_{defective} + E_{atom} - E_{pristine}$$

Here, $E_{formation}$ is the vacancy formation energy; $E_{defective}$ is the total energy of BiOCl or Bi_2O_3; E_{atom} is the energy of an isolated Bi, O, or Cl atom; and $E_{pristine}$ is the total energies of BiOCl or Bi_2O_3. On the basis of the equation, the lower the formation energy, the easier the formation of monovacancy.

The work function (Φ) was calculated to determine the minimum energy required for an electron to escape from the surface of a material to the vacuum as follows

$$\Phi = E_{vac} - E_F$$

where E_{vac} and E_F represent the electrostatic potential of vacuum and Fermi levels, respectively.

The adsorption energy (E_{ad}) per H_2O molecule was calculated as follows

$$E_{ad} = E_{com} - E_{sub} - E_{H_2O}$$

where E_{com} E_{sub} is the energy of BiOCl or Bi_2O_3 with or without an H_2O molecule, respectively. E_{H2O} is the energy for one isolated H_2O molecule. A negative magnitude E_{ad} indicated an exothermic adsorption process.

Bader's charge analysis was performed to estimate the charge transfer (ΔQ) between the substrate and the molecule. ΔQ can be defined as

$$\Delta Q = Q_1 - Q_0$$

where Q_0 and Q_1 are the number of electrons occupied by each substrate before and after adsorption. A negative magnitude ΔQ infers that the electrons flow from the substrate to the molecule.

GSH degradation in vitro

First, a final 0.1 mM concentration of GSH solution was mixed with DTNB with a final 0.2 mg/ml concentration. Then, the above solution was treated with the following treatments: (i) US, (ii) BiOCl NSs, (iii) BiOCl/Bi_2O_3 NSs, (iv) BiOCl NSs + US, and (v) BiOCl/Bi_2O_3 NSs + US. The final concentration of NSs was 0.1 mg/ml. US treatment conditions were 1 MHz, 0.8 W cm^{-2}, and 50% duty cycle. During the 30-min reaction, the absorbance of DTNB was detected every 5 min using the UV-vis spectroscopy.

·OH generation in vitro

MB was applied as a ·OH indicator for detecting the generation of BiOCl NSs and BiOCl/Bi_2O_3 NSs. The ·OH production performance was seen in the following groups: (i) US, (ii) BiOCl NSs, (iii) BiOCl/Bi_2O_3 NSs, (iv) BiOCl NSs + US, and (v) BiOCl/Bi_2O_3 NSs + US. The final concentration of NSs was 0.1 mg/ml. US treatment conditions were 1 MHz, 0.8 W cm^{-2}, and 50% duty cycle. During the 30-min reaction, the absorbance MB was recorded every 5 min through UV-vis spectroscopy.

$\cdot O_2^-$ generation in vitro

The $\cdot O_2^-$-generating ability of BiOCl NSs and BiOCl/Bi_2O_3 NSs within the suspension was evaluated through the probe of DPBF. The $\cdot O_2^-$ production performance was detected through the following group: (i) US, (ii) BiOCl NSs, (iii) BiOCl/Bi_2O_3 NSs, (iv) BiOCl NSs + US, (v) BiOCl/Bi_2O_3 NSs + US, (vi) BiOCl NSs + US-hypoxia, and (vii) BiOCl/Bi_2O_3 NSs + US-hypoxia. The final concentration of NSs was 0.1 mg/ml. US treatment conditions were 1 MHz, 0.8 W cm^{-2}, and 50% duty cycle. During the 30-min reaction, the DPBF absorbance was recorded every 5 min through UV-vis spectroscopy.

CO generation in vitro

The CO-generating ability of BiOCl NSs and BiOCl/Bi_2O_3 NSs was evaluated in the suspension using a tandem gas chromatograph (Agilent GC-7890) by observing and comparing the chromatographic peaks with various standards. The CO production performance was detected with the following group: (i) US, (ii) BiOCl NSs, (iii) BiOCl/Bi_2O_3 NSs, (iv) BiOCl NSs + US, (v) BiOCl/Bi_2O_3 NSs + US, (vi) BiOCl NSs + US-hypoxia, and (vii) BiOCl/Bi_2O_3 NSs + US-hypoxia. The final concentration of NSs was 0.1 mg/ml. US treatment conditions were 1 MHz, 0.8 W cm^{-2}, and 50% duty cycle.

Biocompatibility of NSs in vitro

The biocompatibility of BiOCl NSs and BiOCl/Bi_2O_3 NSs was tested with normal human and cancer cell lines, including the human embryonic kidney cells (HEK293), normal human liver cells (HL-7702), normal human mammary epithelial cells (MCF-10A), human breast cancer cells (MCF-7), and human liver cancer cells (HepG2). The cells were seeded into two 96-well plates at a density of 5000 cells in every well and incubated for 24 hours. Afterward, BiOCl NSs and BiOCl/Bi_2O_3 NSs (0 to 150 μg/ml) were added to the above-mentioned normal cells and coincubated for another 24 hours. Last, cell viabilities were detected using the MTT cell viability assay.

Intracellular ROS generation

The ROS probe, dihydroethidium (DHE), tested the intracellular generation of ROS through confocal laser scanning microscopy (CLSM) imaging. HepG2 cells were seeded into 96-well plates for 24 hours (37°C, 5% CO_2). Then, the cells were treated with the following: (i) US, (ii) BiOCl NSs, (iii) BiOCl/Bi_2O_3 NSs, (iv) BiOCl NSs + US, and (v) BiOCl/Bi_2O_3 NSs + US. The final concentration of NSs was 0.1 mg/ml. The condition for US treatment was 1 MHz, 0.8 W cm^{-2}, and 50% duty cycle, for 5 min. Afterward, DHE with the final 0.2 μM concentration was added to the above-treated cells. After 1-hour incubation, the treated HepG2 cells were washed thrice with PBS. Last, the intracellular ROS concentration was determined using CLSM and flow cytometry.

Intracellular CO generation

The CO probe, COP-1, tested the intracellular generation of CO through CLSM imaging. The HepG2 cells were seeded into 96-well plates for 24 hours (37°C, 5% CO_2). Then, the cells were treated using the following: (i) US, (ii) BiOCl NSs, (iii) BiOCl/Bi_2O_3 NSs, (iv) BiOCl NSs + US, and (v) BiOCl/Bi_2O_3 NSs + US. The final concentration of NSs was 0.1 mg/ml. The US treatment condition was 1 MHz, 0.8 W cm^{-2}, and 50% duty cycle, for 5 min. After that, a CO probe with the final 1 μM concentration was added to the above-treated cells. After 0.5-hour incubation, the treated HepG2 cells were washed three times with PBS. Last, the intracellular ROS concentration was determined using CLSM and flow cytometry.

Intracellular DNA damage

The phosphorylated H2AX is the marker of early DNA damage. Cellular phosphorylated H2AX (γH2AX) under different treatments were determined using Alexa Fluor 647 mouse anti-H2AX (pS139) antibody to characterize the early DNA damage. Briefly, HepG2 cells were seeded into the 96-well plates for 24 hours (37°C, 5% CO_2). Then, the cells were treated as follows: (i) US, (ii) BiOCl NSs, (iii) BiOCl/Bi_2O_3 NSs, (iv) BiOCl NSs + US, and (v) BiOCl/Bi_2O_3 NSs + US. The final concentration of NSs was 0.1 mg/ml. The condition for US treatment was 1 MHz, 0.8 W cm^{-2}, and 50% duty cycle, for 5 min. Then, the cells were stained using a 5 μl per test of Alexa Fluor 647 mouse anti-H2AX (pS139) antibody based on the manufacturer's instructions. After incubating for 30 min, the treated HepG2 cells were washed thrice with PBS. Last, the cellular phosphorylated H2AX (γH2AX) was evaluated with CLSM and flow cytometry.

Detection of intracellular mitochondrial membrane potential

A mitochondrial membrane potential assay kit with JC-1 was used to detect the mitochondrial membrane potential. HepG2 cells were seeded into 96-well plates for 24 hours (37°C, 5% CO_2). Then, the cells were treated with the following: (i) US, (ii) BiOCl NSs, (iii) BiOCl/Bi_2O_3 NSs, (iv) BiOCl NSs + US, and (v) BiOCl/Bi_2O_3 NSs + US. The final concentration of NSs was 0.1 mg/ml. The condition for US treatment was 1 MHz, 0.8 W cm^{-2}, and 50% duty cycle, for 5 min. Then, 1 ml of JC-1 staining solution was added to each well, mixed, and incubated at 37°C for 20 min. Then, the supernatant was aspirated and washed twice using the JC-1 staining buffer (1×). Last, the mitochondrial membrane potential was determined with CLSM and flow cytometry.

Antitumor therapy in vitro

The MCF-7 and HepG2 cells were incubated into 96-well plates for 24 hours (37°C, 5% CO_2). Subsequently, the old culture medium was replaced with a fresh one and treated within the following groups: (i) BiOCl NSs, (ii) BiOCl/Bi_2O_3 NSs, (iii) BiOCl NSs + US, and (iv) BiOCl/Bi_2O_3 NSs + US. The final concentration of NSs was 0.1 mg/ml. The condition for US treatment was 1 MHz, 0.8 W cm^{-2}, and 50% duty cycle, for 5 min. The US treatment was carried out after NSs treated for 12 hours and removed from plates using PBS after washing thrice. Last, cell viabilities were determined using MTT assay (Life Technologies) based on the manufacturer's instructions. In addition, the flow cytometry was applied to analyze the cell apoptosis under different treatments.

Pharmacokinetic study

To understand the pharmacokinetics of BiOCl/Bi_2O_3 NSs in vivo, 200 μl of Cy5.5-PEG-NH_2–modified BiOCl/Bi_2O_3 NSs was intravenously injected within healthy C57BL/6 mice, and the dose of BiOCl/Bi_2O_3 NSs was 4 mg/kg. Afterward, 20 μl of blood was taken from the mice at different time intervals. Then, the fluorescence intensity of Cy5.5-PEG-NH_2–modified BiOCl/Bi_2O_3 NSs in blood was detected through a BioTek microplate reader.

Xenograft tumor model

All animal experiments were conducted on the basis of the Guidelines for the Care and Use of Laboratory Animals of Tianjin University. The experiments were approved by the Animal Ethics Committee of the Tianjin University Laboratory Animal Center (Tianjin, China). This study used 6- to 8-week-old female Balb/c nude mice and female C57BL/6 mice (purchased from Tianjin Medical Laboratory Animal Center, Tianjin, China). Five mice were kept in one cage with free access to food and water. The cages with five mice per cage were placed inside conventional rooms with controlled photoperiod (07:00 to 19:00 white light, ± 200 lux at 1 m above the floor; 19:00 to 07:00 red light, ± 5 lux at 1 m), temperature (20° to 22°C), relative humidity (50 to 60%), and ventilation (15 air changes $hour^{-1}$). The HepG2 tumor models were established using the subcutaneous cell injection (2×10^6 cells in 100 μl of serum-free cell medium) within the right hind leg of Balb/c nude mice. When the size of the tumors reached about 100 mm^3, the mice were divided randomly into different groups for various treatments.

Fluorescence imaging and biodistribution study in vivo

BiOCl/Bi_2O_3 NSs with Cy5.5-PEG-NH_2 was intravenously injected into the HepG2 tumor–bearing mice through the tail vein. Maestro2 in vivo imaging system detected the fluorescence at different times after injection. Subsequently, the major organs (e.g., heart, liver, spleen, lung, and kidney) and tumors of mice were obtained and imaged after the mice were killed through cervical dislocation. The fluorescence intensity of Cy5.5 was measured using ImageJ to depict the accumulation of NSs in tumors and organs. Then, the intensity values were divided using the weight (grams) of each organ. For accurate quantitative determination of the biodistribution of BiOCl/Bi_2O_3 NSs, the HepG2 tumor–bearing mice were intravenously injected with BiOCl/Bi_2O_3 NSs (200 μl per mouse; dosage, 5 mg kg^{-1}). The control group was intravenously injected with 200 μl of PBS. The mice were euthanized, and the major organs, including heart, liver, spleen, lungs, kidney, and tumor, were collected after 24 hours after injection. Those organs were added with 10 ml of aqua regia and heated to 200°C for 3 hours. After being cooled to room temperature, each sample was diluted to 10 ml using deionized water and passed through a 0.22-μm filter to remove undigested tissues. The amount of Fe was measured using ICP atomic emission spectrometry.

CT imaging in vivo

A small mouse x-ray CT (Gamma Medica-Ideas) was used to in vivo CT imaging. Imaging parameters were as follows: field of view, 80 mm by 80 mm; slice thickness, 154 μm; effective pixel size, 50 μm; tube voltage, 80 kV; tube current, 270 μA. The reconstruction was done by using the filtered back projection method. The reconstruction kernel used a Feldkamp cone beam correction and SheppLogan filter. The CT images were analyzed using amira 4.1.2. In detail, tumor-bearing nude mice were intravenously injected with 200 μl of BiOCl/Bi_2O_3 NSs (10 mg/ml) before imaging. After 12 and 24 hours, tumor-bearing mice were imaged by a small animal x-ray CT. The mice whole-body 360° scan lasted about 20 min under isophane anesthesia.

Antitumor therapy in vivo

The HepG2 tumor–bearing mice were randomly divided into six treatment groups with five mice for each group as follows: (i) PBS, (i) US, (ii) BiOCl NSs, (iv) BiOCl/Bi_2O_3 NSs, (v) BiOCl NSs + US, and (vi) BiOCl/Bi_2O_3 NSs + US. The injection dose of NSs was 4 mg/kg. The NSs were reconstituted within PBS solution with a 0.2 mg/ml concentration for administration into the mice and delivered as a

single bolus dose. The condition for US treatment was 1 MHz, 0.8 W cm^{-2}, and 50% duty cycle. The exposure time of treatment with the US was 10 min. For groups 5 and 6, the mice were exposed to the US successively at 24 hours after injection. The tumor size and body weight of each group were measured using a digital scale and caliper every 2 days for 14 days during the treatment. Then, the tumor volume was calculated.

Biosafety in vivo

Healthy C57BL/6 mice were intravenously injected with BiOCl/Bi_2O_3 NSs in PBS (10 mg/ml) to conduct the biosafety experiment. Twenty-four hours after injection, the representative cytokines, including IL-6, TNF-α, and IFN-γ, were determined using enzyme-linked immunosorbent assay based on the manufacturer's instructions. Subsequently, the relative indexes in blood, including BUN, creatinine, albumin, total protein, ALT, and AST, were measured to evaluate the biocompatibility and immune response of BiOCl/Bi_2O_3 NSs. After 1 month of treatment, the main organs (heart, liver, spleen, lung, and kidneys) were retrieved for analysis using H&E staining.

SUPPLEMENTARY MATERIALS

Supplementary material for this article is available at https://science.org/doi/10.1126/sciadv.abo7372

View/request a protocol for this paper from *Bio-protocol*.

REFERENCES AND NOTES

1. S. Afewerki, A. Cordova, Combinations of aminocatalysts and metal catalysts: A powerful cooperative approach in selective organic synthesis. *Chem. Rev.* **116**, 13512–13570 (2016).
2. Z. Zheng, X. Ma, X. Cheng, K. Zhao, K. Gutman, T. Li, L. Zhang, Homogeneous gold-catalyzed oxidation reactions. *Chem. Rev.* **121**, 8979–9038 (2021).
3. X. Lang, J. Zhao, X. Chen, Cooperative photoredox catalysis. *Chem. Soc. Rev.* **45**, 3026–3038 (2016).
4. G. Filippini, F. Longobardo, L. Forster, A. Criado, G. Di Carmine, L. Nasi, C. D'Agostino, M. Melchionna, P. Fornasiero, M. Prato, Light-driven, heterogeneous organocatalysts for C–C bond formation toward valuable perfluoroalkylated intermediates. *Sci. Adv.* **6**, eabc9923 (2020).
5. W. Wei, P. Sun, Z. Li, K. Song, W. Su, B. Wang, Y. Liu, J. Zhao, A surface-display biohybrid approach to light-driven hydrogen production in air. *Sci. Adv.* **4**, eaap9253 (2018).
6. L. Fan, C. Xia, F. Yang, J. Wang, H. Wang, Y. Lu, Strategies in catalysts and electrolyzer design for electrochemical CO_2 reduction toward C_{2+} products. *Sci. Adv.* **6**, eaay3111 (2020).
7. B. Yang, Y. Chen, J. Shi, Nanocatalytic medicine. *Adv. Mater* **31**, 1901778 (2019).
8. Y. Kang, L. Lei, C. Zhu, H. Zhang, L. Mei, X. Ji, Piezo-photocatalytic effect mediating reactive oxygen species burst for cancer catalytic therapy. *Mater. Horiz.* **8**, 2273–2285 (2021).
9. N. Kong, H. Zhang, C. Feng, C. Liu, Y. Xiao, X. Zhang, L. Mei, J. S. Kim, W. Tao, X. Ji, Arsenene-mediated multiple independently targeted reactive oxygen species burst for cancer therapy. *Nat. Commun.* **12**, 4777 (2021).
10. Y.-J. Lin, I. Khan, S. Saha, C.-C. Wu, S. R. Barman, F.-C. Kao, Z.-H. Lin, Thermocatalytic hydrogen peroxide generation and environmental disinfection by Bi_2Te_3 nanoplates. *Nat. Commun.* **12**, 180 (2021).
11. X. Ji, Y. Kang, T. Fan, Q. Xiong, S. Zhang, W. Tao, H. Zhang, An antimonene/Cp*Rh(phen)Cl/black phosphorus hybrid nanosheet-based Z-scheme artificial photosynthesis for enhanced photo/bio-catalytic CO_2 reduction. *J. Mater. Chem. A* **8**, 323–333 (2020).
12. X. Ji, L. Ge, C. Liu, Z. Tang, Y. Xiao, W. Chen, Z. Lei, W. Gao, S. Blake, D. De, B. Shi, X. Zeng, N. Kong, X. Zhang, W. Tao, Capturing functional two-dimensional nanosheets from sandwich-structure vermiculite for cancer theranostics. *Nat. Commun.* **12**, 1124 (2021).
13. C. Pan, M. Ou, Q. Cheng, Y. Zhou, Y. Yu, Z. Li, F. Zhang, D. Xia, L. Mei, X. Ji, Z-scheme heterojunction functionalized pyrite nanosheets for modulating tumor microenvironment and strengthening photo/chemodynamic therapeutic effects. *Adv. Funct. Mater.* **30**, 1906466 (2020).
14. C. Pan, Z. Mao, X. Yuan, H. Zhang, L. Mei, X. Ji, Heterojunction nanomedicine. *Adv. Sci.*, 2105747 (2022).
15. B. Yang, Y. Chen, J. Shi, Reactive oxygen species (ROS)-based nanomedicine. *Chem. Rev.* **119**, 4881–4985 (2019).
16. K. G. Anderson, I. M. Stromnes, P. D. Greenberg, Obstacles posed by the tumor microenvironment to T cell activity: A case for synergistic therapies. *Cancer Cell* **31**, 311–325 (2017).
17. T. Wu, Y. Dai, Tumor microenvironment and therapeutic response. *Cancer Lett.* **387**, 61–68 (2017).
18. Y. Dai, C. Xu, X. Sun, X. Chen, Nanoparticle design strategies for enhanced anticancer therapy by exploiting the tumour microenvironment. *Chem. Soc. Rev.* **46**, 3830–3852 (2017).
19. J. Liu, Q. Chen, L. Feng, Z. Liu, Nanomedicine for tumor microenvironment modulation and cancer treatment enhancement. *Nano Today* **21**, 55–73 (2018).
20. L. Gu, D. J. Mooney, Biomaterials and emerging anticancer therapeutics: Engineering the microenvironment. *Nat. Rev. Cancer* **16**, 56–66 (2016).
21. Y. Kang, Z. Li, Y. Yang, Z. Su, X. Ji, S. Zhang, Antimonene nanosheets-based Z-scheme heterostructure with enhanced reactive oxygen species generation and photothermal conversion efficiency for photonic therapy of cancer. *Adv. Healthc. Mater.* **10**, 2001835 (2021).
22. M. Ou, C. Pan, Y. Yu, X. Wang, Y. Zhou, H. Zhang, Q. Cheng, M. Wu, X. Ji, L. Mei, Two-dimensional highly oxidized ilmenite nanosheets equipped with Z-scheme heterojunction for regulating tumor microenvironment and enhancing reactive oxygen species generation. *Chem. Eng. J.* **390**, 124524 (2020).
23. J. Low, J. Yu, M. Jaroniec, S. Wageh, A. A. Al-Ghamdi, Heterojunction Photocatalysts. *Adv. Mater.* **29**, 1601694 (2017).
24. W. Zeng, H. Zhang, X. Yuan, T. Chen, Z. Pei, X. Ji, Two-dimensional nanomaterial-based catalytic medicine: Theories, advanced catalyst and system design. *Adv. Drug Deliv. Rev.* **184**, 114241 (2022).
25. J. Low, C. Jiang, B. Cheng, S. Wageh, A. A. Al-Ghamdi, J. Yu, A review of direct Z-scheme photocatalysts. *Small Methods* **1**, 1700080 (2017).
26. C. Bae, H. Thi Anh, H. Kim, S. Lee, S. Lim, M. Kim, H. Yoo, J. M. Montero-Moreno, J. H. Park, H. Shin, Bulk layered heterojunction as an efficient electrocatalyst for hydrogen evolution. *Sci. Adv.* **3**, e1602215 (2017).
27. D. Chu, Y. H. Lee, E. K. Kim, Selective control of electron and hole tunneling in 2D assembly. *Sci. Adv.* **3**, e1602726 (2017).
28. W. Zhang, A. R. Mohamed, W.-J. Ong, Z-scheme photocatalytic systems for carbon dioxide reduction: Where are we now? *Angew. Chem. Int. Ed. Engl.* **59**, 22894–22915 (2020).
29. A. Kumar, P. Raizada, P. Singh, R. V. Saini, A. K. Saini, A. Hosseini-Bandegharaei, Perspective and status of polymeric graphitic carbon nitride based Z-scheme photocatalytic systems for sustainable photocatalytic water purification. *Chem. Eng. J.* **391**, 123496 (2020).
30. Y. Chen, Z. Fan, Z. Zhang, W. Niu, C. Li, N. Yang, B. Chen, H. Zhang, Two-dimensional metal nanomaterials: Synthesis, properties, and applications. *Chem. Rev.* **118**, 6409–6455 (2018).
31. C. Tan, X. Cao, X.-J. Wu, Q. He, J. Yang, X. Zhang, J. Chen, W. Zhao, S. Han, G.-H. Nam, M. Sindoro, H. Zhang, Recent advances in ultrathin two-dimensional nanomaterials. *Chem. Rev.* **117**, 6225–6331 (2017).
32. Y. Guo, K. Xu, C. Wu, J. Zhao, Y. Xie, Surface chemical-modification for engineering the intrinsic physical properties of inorganic two-dimensional nanomaterials. *Chem. Soc. Rev.* **44**, 637–646 (2015).
33. X. Peng, L. Peng, C. Wu, Y. Xie, Two dimensional nanomaterials for flexible supercapacitors. *Chem. Soc. Rev.* **43**, 3303–3323 (2014).
34. K. Shehzad, Y. Xu, C. Gao, X. Duan, Three-dimensional macro-structures of two-dimensional nanomaterials. *Chem. Soc. Rev.* **45**, 5541–5588 (2016).
35. Y. Wang, L. Wang, X. Zhang, X. Liang, Y. Feng, W. Feng, Two-dimensional nanomaterials with engineered bandgap: Synthesis, properties, applications. *Nano Today* **37**, 101059 (2021).
36. D. Akinwande, N. Petrone, J. Hone, Two-dimensional flexible nanoelectronics. *Nat. Commun.* **5**, 5678 (2014).
37. C. Tan, H. Zhang, Wet-chemical synthesis and applications of non-layer structured two-dimensional nanomaterials. *Nat. Commun.* **6**, 7873 (2015).
38. S. R. Neufeldt, M. S. Sanford, Controlling site selectivity in palladium-catalyzed C–H bond functionalization. *Acc. Chem. Res.* **45**, 936–946 (2012).
39. R. K. B. Karlsson, A. Cornell, Selectivity between oxygen and chlorine evolution in the chlor-alkali and chlorate processes. *Chem. Rev.* **116**, 2982–3028 (2016).
40. J. Fu, K. Jiang, X. Qiu, J. Yu, M. Liu, Product selectivity of photocatalytic CO_2 reduction reactions. *Mater. Today* **32**, 222–243 (2020).
41. A. Sahu, I. Kwon, G. Tae, Improving cancer therapy through the nanomaterials-assisted alleviation of hypoxia. *Biomaterials* **228**, 119578 (2020).
42. X. Jing, F. Yang, C. Shao, K. Wei, M. Xie, H. Shen, Y. Shu, Role of hypoxia in cancer therapy by regulating the tumor microenvironment. *Mol. Cancer* **18**, 157 (2019).
43. Z. Tang, Y. Liu, M. He, W. Bu, Chemodynamic therapy: Tumour microenvironment-mediated fenton and fenton-like reactions. *Angew. Chem. Int. Ed. Engl.* **58**, 946–956 (2019).
44. J. Zhu, S. Mu, Defect engineering in carbon-based electrocatalysts: Insight into intrinsic carbon defects. *Adv. Funct. Mater.* **30**, 2001097 (2020).
45. D. Yan, Y. Li, J. Huo, R. Chen, L. Dai, S. Wang, Defect chemistry of nonprecious-metal electrocatalysts for oxygen reactions. *Adv. Mater.* **29**, 1606459 (2017).

46. H. Maeda, Toward a full understanding of the EPR effect in primary and metastatic tumors as well as issues related to its heterogeneity. *Adv. Drug Deliv. Rev.* **91**, 3–6 (2015).
47. S. K. Golombek, J.-N. May, B. Theek, L. Appold, N. Drude, F. Kiessling, T. Lammers, Tumor targeting via EPR: Strategies to enhance patient responses. *Adv. Drug Deliv. Rev.* **130**, 17–38 (2018).
48. J. Fang, W. Islam, H. Maeda, Exploiting the dynamics of the EPR effect and strategies to improve the therapeutic effects of nanomedicines by using EPR effect enhancers. *Adv. Drug Deliv. Rev.* **157**, 142–160 (2020).
49. J. Shi, P. W. Kantoff, R. Wooster, O. C. Farokhzad, Cancer nanomedicine: Progress, challenges and opportunities. *Nat. Rev. Cancer* **17**, 20–37 (2017).
50. Y. Min, J. M. Caster, M. J. Eblan, A. Z. Wang, Clinical translation of nanomedicine. *Chem. Rev.* **115**, 11147–11190 (2015).
51. E. K.-H. Chow, D. Ho, Cancer nanomedicine: From drug delivery to imaging. *Sci. Transl. Med.* **5**, 216rv4 (2013).
52. C. von Roemeling, W. Jian, C. K. Chan, I. L. Weissman, B. Y. S. Kim, Breaking down the barriers to precision cancer nanomedicine. *Trends Biotechnol.* **35**, 159–171 (2017).

Acknowledgments

Funding: This study was financially supported by a grant from the National Natural Science Foundation of China (grant no. 32071322), National Natural Science Funds for Excellent Young Scholar (grant no. 32122044 and 32000815), and Technology and Innovation Commission of Shenzhen Municipality (grant no. JCYJ20210324113004010).

Author contributions: X.J. designed and supervised the project. X.J. and L.C. designed the experimental strategies. L.C., Yang Wang, Z.M., Ying Wang, Y.K., and L.M. performed the experiments and analyzed the data. X.J., Yang Wang, and Y.K. wrote the manuscript.
Competing interests: The authors declare that they have no competing interests. **Data and materials availability:** All data needed to evaluate the conclusions in the paper are present in the paper and/or the Supplementary Materials.

Submitted 22 February 2022
Accepted 15 August 2022
Published 30 September 2022
10.1126/sciadv.abo7372